Geophysical & Astrophysical Fluid Dynamics

Publication details, including instructions for authors and subscription information:
http://www.tandfonline.com/loi/ggaf20

Nonlinear baroclinic equilibration at finite supercriticality

J. G. Esler [a] & B. T. Willcocks [a]

[a] Department of Mathematics , University College London , 25 Gower Street, London , WC1E 6BT , UK

Published online: 24 Jan 2012.

To cite this article: J. G. Esler & B. T. Willcocks (2012) Nonlinear baroclinic equilibration at finite supercriticality, Geophysical & Astrophysical Fluid Dynamics, 106:3, 320-350, DOI: 10.1080/03091929.2011.637033

To link to this article: http://dx.doi.org/10.1080/03091929.2011.637033

Geophysical and Astrophysical Fluid Dynamics
Vol. 106, No. 3, June 2012, 320–350

Taylor & Francis
Taylor & Francis Group

Nonlinear baroclinic equilibration at finite supercriticality

J. G. ESLER* and B. T. WILLCOCKS

Department of Mathematics, University College London, 25 Gower Street, London, WC1E 6BT, UK

(*Received 1 June 2011; in final form 24 August 2011; first published online 24 January 2012*)

The nonlinear equilibration of finite amplitude baroclinic waves in Phillips two-layer model is investigated at finite supercriticality. The aims are to quantify the robustness and relevance of the nonlinear theory of Warn, Gauthier and Pedlosky (WGP) for the evolution of the developing baroclinic wave, and to assess the tightness of pseudomomentum and improved pseudoenergy bounds for disturbance amplitude and energy. A high-resolution numerical model is used to perform a parameter sweep in (β, W)-space, where β is the inverse criticality of the initial flow, and W is the ratio of the channel width to the (internal) Rossby radius. At low supercriticalities, the main predictions of WGP are found to be accurate at short times, but at long times the fully nonlinear results are found to diverge from WGP's solution. The mechanism for equilibration involves the elimination of the lower layer potential vorticity (PV) gradient, but as the supercriticality increases this is achieved by the roll-up of a train of opposite-signed vortices, rather than by coarse-grain PV homogenization as in WGP. Peak wave amplitudes are typically $\approx$90% of the maximum attainable under the pseudomomentum bound. New formulae are given for the pseudoenergy bound on disturbance energy which, unlike the WGP solution and the pseudomomentum bound, have non-trivial dependence on W. A detailed assessment is made of the extent to which these bounds are attained.

Keywords: baroclinic instability; nonlinear equilibration; critical layers;

1. Introduction

Determining and quantifying the mechanisms by which unstable baroclinic waves equilibrate is a question of central importance in dynamical meteorology, oceanography and theoretical fluid dynamics. Theoretical interest in the problem was sparked by the influential analytical solutions of Drazin (1970) for the Eady model, and particularly that of Pedlosky (1970) for Phillips two-layer model. In the latter case an initially unstable baroclinic wave undergoes a time-periodic nonlinear oscillation in which eddy energy is repeatedly extracted from and returned to the mean flow. Pedlosky's solution, characterised by these reversible exchanges of energy, was for a time considered an archetype of an idealised baroclinic lifecycle in a channel flow.

*Corresponding author. Email: gavin@math.ucl.ac.uk

Geophysical and Astrophysical Fluid Dynamics
ISSN 0309-1929 print/ISSN 1029-0419 online
http://dx.doi.org/10.1080/03091929.2011.637033

However, the numerical experiments of Boville (1981) revealed a quantitative discrepancy with Pedlosky's solution near minimum critical shear, and the reversible oscillations were not observed. The reason, as was clarified by Pedlosky (1982a, b), is that at minimum critical shear higher harmonics of the fundamental wave are resonantly excited in the lower layer, and the excited harmonics then interact with the fundamental at leading order in the solution.

A physical explanation for the resonant excitation of harmonics follows from the observation that in the lower layer, the frequency of the fundamental wave vanishes relative to the mean flow and the entire layer is a Rossby wave critical layer (see, e.g. Maslowe 1986). Pedlosky (1982b) derived an infinite-dimensional dynamical system for the evolution of the critical layer, and by numerical solution of a truncated subset of the governing equations deduced some properties of the flow. In particular, the equilibrated state of the system was identified with potential vorticity (PV) homogenization throughout the lower layer. PV homogenization is now understood as a fundamental process influencing the equilibration of a much wider class of geophysical flows (e.g. Rhines and Young 1983).

An elegant and attractive analytical solution for the problem was later given by Warn and Gauthier (1989; hereafter WG89). Pedlosky's relatively unwieldy system of equations were recast as a pair of integro-differential equations, which are integrable. Henceforth, this solution will be referred to as the Warn–Gauthier–Pedlosky (WGP) solution. In the WGP solution, although the evolution of the lower layer PV field remains transient, the fundamental wave approaches an equilibrated amplitude. In these exact equations, the lower layer PV distribution undergoes a cascade to smaller scales, while the fundamental wave in the upper layer "sees" only the large-scale "coarse-grain" lower layer PV. Hence equilibration is possible in the upper layer while the lower layer remains transient.

WGP's theory is valid only for initial flows that are weakly unstable, i.e. in the limit of infinitesimal supercriticality. An alternative approach to investigating unstable baroclinic flows at finite supercriticality was pioneered by Shepherd, who adapted the nonlinear stability theorems of Arnol'd (1966) to the specific situation of an initially unstable baroclinic flow in Phillips model. Both bounds on perturbation enstrophy (Shepherd 1988), obtained by the momentum-Casimir method, and perturbation energy (Shepherd 1993), obtained by the energy–momentum-Casimir method (see, e.g. Shepherd 1990, for a comprehensive review), lead to useful constraints on the fully nonlinear evolution.

Although the above solutions and bounds are clearly of great pedagogical value, there remain numerous open questions as to their relevance to real flows in experiments and the atmosphere and ocean. One aim of this work is to create a bridge between these results and more realistic flows using idealised high-resolution numerical experiments. To our knowledge, despite its importance as a textbook paradigm, there has been no systematic numerical investigation of baroclinic instability in Phillips model at finite criticality since WG89's work. A second aim is to assess the extent to which Warn and Gauthier's (1989) (WGP) solution is realised and Shepherd's bounds are attained. As part of the process of achieving these aims, new and simpler derivations of the WGP solution and bounds are presented.

The assessment of WGP and Shepherd's bounds will determine whether or not they present a reasonably accurate qualitative and quantitative description of a wider class

of flows at finite supercriticality. Specifically, the focus will be on answering the following questions:

- To what extent is the WGP solution realised at finite supercriticality? For example, it has been argued (Gauthier 1990, Shepherd 1993) that at finite criticality the Rossby wave critical layer either will not form or will occupy only part of the lower layer of the channel. It is thought that the original Pedlosky (1970) solution might then be more relevant. How accurate are the WGP predictions for peak and equilibrated wave amplitudes at finite criticality?
- Is the WGP solution stable on all timescales? For example, Killworth and McIntyre (1985) argued that idealised Rossby wave critical layers (Stewartson 1978, Warn and Warn 1978) are subject to a secondary barotropic instability, the existence of which was verified numerically by Haynes (1985, 1989).
- Is the mechanism of nonlinear baroclinic equilibration in the WGP solution, i.e. homogenization of coarse-grain PV in the lower layer, essentially unaltered at finite criticality?
- The perturbation enstrophy bound given by Shepherd (1988) translates into a bound on the amplitude of the fundamental wave in the upper layer. To what extent is this bound, which is independent of the ratio of the channel width to the internal Rossby radius (W hereafter), attained by the disturbances? Does the maximum wave amplitude attained depend on W?
- To what extent are the perturbation energy bounds of Shepherd (1993) attained by the disturbances? Can these bounds be improved upon? Does the non-trivial dependence on W of the perturbation energy bound indicate the nature of the sensitivity of fully nonlinear flows to W?

In section 2 the set-up of the numerical experiments will be described, and in section 3 the WGP solution and Shepherd's results will be reviewed. A new formula for the perturbation energy bound is given, and a variational approach is used to improve the bound further. In section 4, the results of the numerical experiments are compared with the predictions of the WGP theory and both Shepherd's bounds and the new results. In section 5, conclusions are drawn and the questions posed above are answered.

2. Experimental set-up and numerical model

2.1. *Baroclinic lifecycles in Phillips two-layer model*

For definiteness, throughout this work, the focus will be on baroclinic lifecycles in a particular set-up as follows. The model adopted is the quasi-geostrophic, two-layer Phillips model (Phillips 1951, 1954) which describes fluid motion in a re-circulating channel between rigid sidewalls at the fixed latitudes $y = \pm L_y/2$. It is assumed that the channel length L_x is effectively infinite, although particular assumptions to be made about the nature of the flow will permit the use of periodic boundary conditions in the numerical implementation, as will be described below. The geometry is relevant to a re-circulating atmosphere, a rotating annulus or an oceanic channel, under the assumption that zonal wavenumber discretization effects, due to the periodicity of the re-circulating domain, are not strongly felt.

Under the β-plane approximation, the channel is subject to differential rotation at the rate $f/2$ where $f=f_0+\beta^* y$. The upper and lower layers, to be henceforth denoted with subscripts 1 and 2 respectively, are each of undisturbed depth H and have densities ρ_1 and ρ_2 ($\rho_1<\rho_2$). The Boussinesq approximation $\Delta=2(\rho_2-\rho_1)/(\rho_1+\rho_2)\ll 1$ is adopted, meaning that an effective gravity $g'=g\Delta$ acts on the interface between the two layers. The equations of motion are then identical whether the upper layer is bounded by a rigid lid, as in an annulus experiment, or has a free surface, as in the oceanic situation.

The basic flow to be considered is that of uniform vertical shear with zonal velocity U in the upper layer and a lower layer at rest. The upper and lower boundaries are assumed frictionless. Nondimensionalizing with horizontal length scale equal to the internal Rossby radius of deformation (see eq. 5.191 of Vallis 2006) $L_D=\sqrt{g'H/2f_0^2}$, vertical length scale H and vertical and horizontal velocity scales U and UH/L_D, respectively, results in equations of motion (e.g. Pedlosky 1987)

$$\left(\partial_t-\psi_{iy}\partial_x+\psi_{ix}\partial_y\right)q_i=0 \qquad\qquad i=1,2\,, \tag{1a}$$

where

$$q_i=\beta y+\nabla^2\psi_i+\tfrac{1}{2}(-1)^i(\psi_1-\psi_2) \tag{1b}$$

is the PV in each layer ($i=1,2$), ψ_i is the geostrophic streamfunction, and the geostrophic velocities are given by $\boldsymbol{u}_i=-\boldsymbol{\nabla}\times\psi_i\boldsymbol{k}$. The boundary conditions at the sidewalls are no-normal flow and the so-called Phillips' boundary condition (conservation of circulation on the boundary)

$$\psi_{ix}=0 \qquad \text{on} \qquad y=\pm W/2, \tag{2a}$$

$$\overline{\psi}_{iyt}=0 \qquad \text{on} \qquad y=\pm W/2. \tag{2b}$$

The two nondimensional parameters appearing in (1) and (2a,b) are the inverse criticality β and the channel width parameter W, which in terms of the physical parameters determining the flow are given by

$$\beta=\frac{\beta^* L_D^2}{U}, \quad W=\frac{L_y}{L_D}. \tag{3}$$

The linear stability problem can be investigated using the ansatz

$$\begin{pmatrix}\psi_1\\ \psi_2\end{pmatrix}=-\begin{pmatrix}y\\ 0\end{pmatrix}+\mathrm{Re}\,\epsilon\begin{pmatrix}1\\ \gamma\end{pmatrix}e^{ik(x-ct)}\sin l\big(y-(W/2)\big), \tag{4}$$

where the first term is the uniform flow, k and l are zonal and meridional wavenumbers, and γ is a complex-valued constant. Note that the values of $l=n\pi/W$ (n integer) are discretized due to the finite channel width. Inserting into (1), and neglecting terms of $O(\epsilon^2)$, leads to the dispersion relation for the phase speed c,

$$c^{\pm}=\frac{1}{2}-\frac{(a^2+\frac{1}{2})}{a^2(a^2+1)}\beta\pm\frac{1}{2a^2(a^2+1)}\left[\beta^2+a^4(a^4-1)\right]^{1/2}, \tag{5}$$

where $a=(k^2+l^2)^{1/2}$ is the total wavenumber. Stability depends on the sign of the square root term in (5), and it is easily verified (Vallis 2006, pp. 271–277) that if $\beta < \frac{1}{2}$ (and $W > 2^{1/4}\pi$) then a band of wavenumbers satisfying

$$\tfrac{1}{2} - \left(\tfrac{1}{4} - \beta^2\right)^{1/2} < a^4 < \tfrac{1}{2} + \left(\tfrac{1}{4} - \beta^2\right)^{1/2} \tag{6}$$

are unstable. The condition $\beta < \frac{1}{2}$ for instability corresponds to a reversal in sign of the lower layer PV gradient and is consistent with the Charney–Stern–Pedlosky sufficient criterion for instability for the flow in question (e.g. sec. 6.4.3 of Vallis 2006).

The baroclinic lifecycles to be considered here are initialized with infinitesimal "noise", in order that a uniform wavetrain consisting of the fastest growing normal mode emerges from that noise. Note that this restriction limits the focus to waves with the gravest cross-channel scale (i.e. $n=1$ so that $l=\pi/W$) which have meridional structure $\sim\cos(\pi y/W)$. There is a hidden assumption here that modulational (envelope or wave-packet forming) instability (see, e.g. Esler 1997) does not play a significant role in the lifecycle, and the developing flow is periodic on the wavelength of the fastest growing mode. The advantage in prescribing the baroclinic cycles as above is that the outcome of each flow is determined by β and W only.

The subsequent flows are strongly constrained by conservation of the following integral quantities, where $\mathcal{D}$ denotes the domain of the channel,

$$M = \int_{\mathcal{D}} yq_1 + yq_2 \,\mathrm{d}\boldsymbol{x} \qquad = \mathrm{LW}^3\beta/6, \tag{7a}$$

$$E = \tfrac{1}{2}\int_{\mathcal{D}} |\boldsymbol{\nabla}\psi_1|^2 + |\boldsymbol{\nabla}\psi_2|^2 + \tfrac{1}{2}(\psi_2-\psi_1)^2 \,\mathrm{d}\boldsymbol{x} \qquad = (\mathrm{LW}/2) + (\mathrm{LW}^3/48), \tag{7b}$$

$$\mathcal{C}[q_1, q_2] = \int_{\mathcal{D}} C_1(q_1) + C_2(q_2)\mathrm{d}\boldsymbol{x}, \tag{7c}$$

where M is Kelvin's impulse, which is closely related to conservation of total zonal momentum, E is the total energy and $\mathcal{C}[q_1, q_2]$ denotes the Casimir invariants, which hold for arbitrary functions C_1 and C_2 and follow from the parcel-wise conservation of PV. The first two integrals have been evaluated for the infinitesimal noise initial conditions, where for definiteness a nondimensional channel length $L(=L_x/L_D)$ has been introduced (assumed much larger than W).

Two important examples of Casimir invariants to be considered below are the upper ($i=1$) and lower ($i=2$) layer planetary† enstrophies

$$Z_i = \tfrac{1}{2}\int_{\mathcal{D}} q_i^2 \,\mathrm{d}\boldsymbol{x} = \frac{\mathrm{LW}^3}{24}\begin{cases} \left(\beta+\frac{1}{2}\right)^2 & i=1, \\ \left(\beta-\frac{1}{2}\right)^2 & i=2. \end{cases} \tag{8}$$

It is important to note that the nondimensionalization adopted above differs from that of previous authors (e.g. Shepherd 1988, Warn and Gauthier 1989) in that the internal Rossby radius, rather than the dimensional channel width, has been used as the horizontal length scale. The advantage of choosing the Rossby radius is that the channel width parameter W scales out of much of the resulting analysis. Note that

†So-called here as the planetary vorticity gradient βy is retained in the definition.

Table 1. Numerical parameter settings for three different numerical resolutions, for simulations with $(\beta, W) = (0.48, 2^{3/4}\pi)$.

Resolution	Fourier modes (x)	Grid points (y)	dt	ν_q
Low (LR)	64	64	5.0×10^{-3}	5.0×10^{-5}
Medium (MR)	128	128	2.5×10^{-3}	2.5×10^{-5}
High (HR)	256	256	1.0×10^{-3}	1.0×10^{-5}

previous works have introduced a degeneracy by retaining three nondimensional variables instead of two, throughout the analysis (e.g. following the precedent of Pedlosky 1987), which arguably somewhat overcomplicates the results. Appendix A describes how to transfer between our approach and those of the cited previous works.

2.2. *Numerical implementation and convergence tests*

Phillips model governing equations (1) are integrated numerically here using a pseudo-spectral/grid-point model, which is essentially that described in Esler and Haynes (1999). The restriction to the infinitesimal noise lifecycle allows the equations to be integrated on the subdomain $(x, y) \in [-\pi/2k_m, 3\pi/2k_m] \times [-W/2, W/2]$, because the resulting dominance of the fastest growing mode guarantees a solution that is $2\pi/k_m$ periodic in the x-direction. A standard Fourier decomposition is employed in the x-direction to take advantage of the periodicity, whereas the grid-point discretization in the y-direction facilitates implementation of the no-normal flow and Phillips' boundary conditions (2a,b).

In order to inhibit the artificial build-up of enstrophy at the grid-scale it is necessary to apply an enstrophy filter. Here, a PV diffusion $\nu_q \nabla^2 q_i$, acting in each layer, is added to the right-hand side of (1). There is no fixed *a priori* rule for setting the value of ν_q required to obtain converged solutions at a particular resolution, rather ν_q is selected according to both the numerical resolution and the strength of the turbulent cascade occurring in the flow under examination. A necessary condition for convergence, satisfied by all of the simulations presented below, is that at all times there is no spurious up-tick in the enstrophy spectrum as the wavenumber approaches that of the grid-scale.

Further convergence tests involve comparison between numerical solutions at different resolutions. PV diffusivities ν_q, time steps δt and details of three corresponding numerical resolutions are presented in table 1. The time step must satisfy the usual Courant–Friedrichs–Lewy criterion and hence scales approximately with the grid-scale. The tabulated values of ν_q are given for a set of simulations with $(\beta, W) = (0.48, 2^{3/4}\pi)$. Slightly higher values of ν_q are necessary at higher supercriticalities (lower β).

Some results are shown in figure 1. The quantity plotted in figure 1(a) is $|A_1^f(t)|$, where $A_i^f(t)$ is a complex wave amplitude defined to be

$$A_i^f(t) = \frac{4}{\mathrm{LW}} \int_{\mathcal{D}} q_i(x, y, t) e^{-\mathrm{i}k_m x} \cos\left(\frac{\pi y}{W}\right) \mathrm{d}\boldsymbol{x}, \quad i = 1, 2, \tag{9}$$

i.e. a measure of the amplitude of the baroclinic wave (with respect to PV) in each layer ($i = 1, 2$) of the model. The upper panel shows the evolution of $|A_1^f(t)|$ at three different numerical resolutions with different values of ν_q (LR, MR and HR in table 1). At early times, but well into the nonlinear stage of the lifecycle, there is excellent agreement between the three. At later times the three solutions begin to diverge, although it is

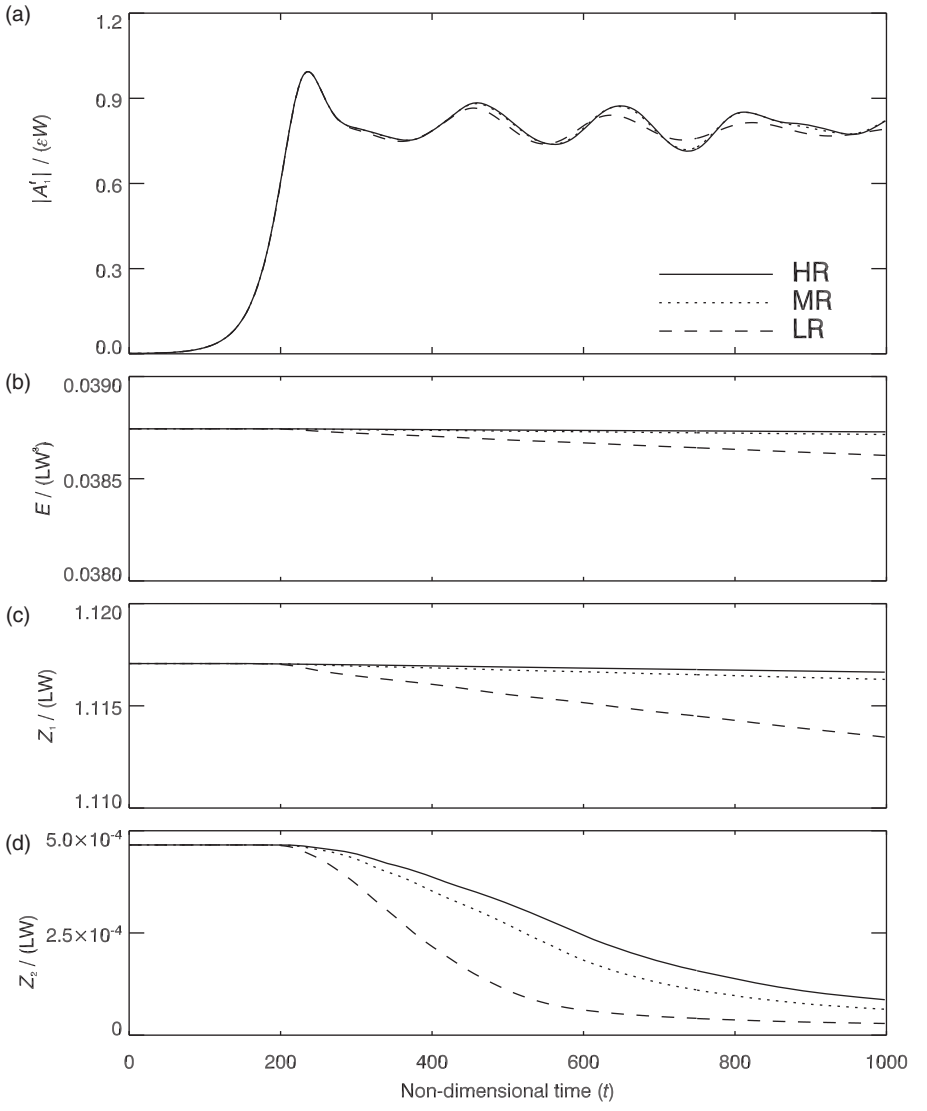

Figure 1. (a) Time evolution of upper layer wave amplitude ($|A_1^f(t)|/\epsilon W$) in a simulation with $(\beta, W) = (0.48, 2^{3/4}\pi)$ for the three numerical resolutions detailed in table 1. (b) Time evolution of total energy E/LW^3 for the same three numerical resolutions. (c, d) As (b) but time evolution of upper and lower layer total planetary enstrophies Z_1/LW and Z_2/LW respectively.

evident that the LR and MR solutions diverge more rapidly than the MR and HR solutions, indicating better-than-linear convergence of the solutions with grid-scale. Figure 1(b) shows the total energy (E/LW^3) of the flow, which in the idealised ($\nu_q = 0$) case is conserved. It is clear that in practice E appears to be conserved almost exactly until well into the nonlinear stage of the lifecycle, after which time the most dissipative LR simulation loses energy at a slow but uniform rate that is an order of magnitude greater than that in the HR simulation. Figures 1(c) and (d) show the upper and lower layer planetary enstrophies (Z_1/LW and Z_2/LW respectively). Z_1 is seen to be well-conserved throughout the simulations, but since PV in the lower layer undergoes a

cascade to smaller scales, Z_2 is well-conserved only up to the time at which the maximum wave amplitude is attained, after which time the scale cascade leads to dissipation of Z_2 in all three simulations. Derived quantities, such as wave pseudomomentum and pseudoenergy to be defined below, are therefore also well-conserved up to the time that the maximum wave amplitude is attained.

It is to be emphasised that figure 1 is representative of a wider class of convergence tests spanning (β, W) parameter space, and is typical of the convergence of the numerical results elsewhere. Further evidence of numerical accuracy will be presented below when the WGP solution is assessed.

3. Analytical theory and bounds on disturbance quantities

3.1. *The WGP analytical theory*

A key objective of this work is to examine the relevance of the WGP solution to flows at finite supercriticality. To facilitate this comparison full details of the WGP solution will be presented next. The main innovation here, compared to (WG89), is the use of the conserved quantities M and Z_1 to provide a fast route to the WGP governing equations. Further simplifications are afforded by restricting the focus to just the infinitesimal noise† baroclinic lifecycle described above. Finally, an effort has been made to minimize the proliferation of new variables, in order to make the presentation of the solution as explicit as possible.

The WGP theory is formulated for flows with supercriticality, defined by

$$\epsilon = (\tfrac{1}{2} - \beta)^{1/2}$$

taken to be formally small ($\epsilon \ll 1$). Power series solutions of (1) are then sought by expanding in ϵ:

$$\psi_i = -y\delta_{i1} + \epsilon\Big(\psi_i^{(0)} + \epsilon\psi_i^{(1)} + \epsilon^2\psi_i^{(2)} + \cdots\Big), \tag{10a}$$

$$q_i = \big(\delta_{1i} - \epsilon^2\big)\, y + \epsilon\Big(q_i^{(0)} + \epsilon q_i^{(1)} + \epsilon^2 q_i^{(2)} + \cdots\Big), \tag{10b}$$

where

$$q_i^{(j)} = \nabla^2\psi_i^{(j)} + (-1)^i\tfrac{1}{2}\Big(\psi_1^{(j)} - \psi_2^{(j)}\Big), \tag{10c}$$

and δ_{ij} is the Kronecker delta. In order to suppress secular terms in the solution, following the method of multiple scales, the terms in the series are allowed to depend on an additional long time variable $\tau = \epsilon t$.

At leading order in ϵ the relevant solution is essentially the linear one for the marginally stable wave with total wavenumber $a = a_m = 2^{-1/4}$. The branch of the linear solution corresponding to the growing mode (see the discussion in WG89) is chosen so that

$$\begin{pmatrix} \psi_1^{(0)} \\ \psi_2^{(0)} \end{pmatrix} = A(\tau)\begin{pmatrix} 1 \\ \gamma_m \end{pmatrix} e^{\mathrm{i}k_m x}\cos\left(\frac{\pi y}{W}\right), \tag{11}$$

†WG89 refer to this lifecycle as their case of "subliminal disturbance".

where the real part is intended, $k_m^2 = a_m^2 - \pi^2/W^2$ and $\gamma_m = \sqrt{2} - 1$. From (5), the real phase speed of the marginally stable wave is zero and thus the leading solution is independent of the fast variable t. Since higher order terms in the series are forced by the leading order solution they can also be taken to be independent of t. The corresponding leading order PV is given by $q_1^{(0)} = -\psi_1^{(0)}$ and, significantly, $q_2^{(0)} = 0$ indicating that the perturbation PV in the lower layer remains an order of magnitude smaller than that in the upper layer. It is nevertheless within the upper layer, where the PV distribution consists of a uniform background gradient plus an $O(\epsilon)$ wave-like perturbation, that the flow remains "Rossby wave-like". In the lower layer both the mean PV gradient and its perturbation are the same amplitude, $O(\epsilon^2)$.

Inserting the expansion (10) into the definitions of M and Z_1 gives

$$Z_1 = Z_1(0) + \epsilon \int_{\mathcal{D}} y q_1^{(0)} \, \mathrm{d}\boldsymbol{x} + \epsilon^2 \int_{\mathcal{D}} y q_1^{(1)} + \tfrac{1}{2}\left(q_1^{(0)}\right)^2 \mathrm{d}\boldsymbol{x} + O(\epsilon^3), \tag{12a}$$

$$M = M(0) + \epsilon \int_{\mathcal{D}} y q_1^{(0)} \, \mathrm{d}\boldsymbol{x} + \epsilon^2 \int_{\mathcal{D}} y q_1^{(1)} + y q_2^{(1)} \, \mathrm{d}\boldsymbol{x} + O(\epsilon^3). \tag{12b}$$

where $Z_1(0)$ and $M(0)$ are the respective initial values given in (7a–c) and (8). Since $M = M(0)$ and $Z_1 = Z_1(0)$ at all times, the terms remaining on the right-hand side are also zero. At $O(\epsilon)$ in both expressions

$$\int_{\mathcal{D}} y q_1^{(0)} \, \mathrm{d}\boldsymbol{x} = 0,$$

which is easily verified upon insertion of (11). At $O(\epsilon^2)$, eliminating the integral of $y q_1^{(1)}$ between the two expressions reveals that

$$\int_{\mathcal{D}} \tfrac{1}{2}(q_1^{(0)})^2 \, \mathrm{d}\boldsymbol{x} = \int_{\mathcal{D}} y q_2^{(1)} \, \mathrm{d}\boldsymbol{x}, \tag{13}$$

which upon insertion of (11) becomes

$$|A(\tau)|^2 = \frac{8}{\mathrm{LW}} \int_{\mathcal{D}} y q_2^{(1)} \, \mathrm{d}\boldsymbol{x}. \tag{14}$$

This is nothing but pseudomomentum conservation for the system. Pseudomomentum invariants are constructed from the linear impulse conservation law $M = M(0)$ (7a) and a suitably chosen Casimir invariant (7c) (see, e.g. Shepherd 1990). Here the chosen Casimir is Z_1. Note that the integral on the right-hand side of (14) measures the change in Kelvin's impulse of the lower layer.

Equation (14) is augmented by the evolution equation for the leading order perturbation PV in the lower layer $q_2^{(1)}$ (recall that $q_2^{(0)} = 0$). Inserting (10) into the governing equation (1), and noting that there is now only slow time-dependence in the problem ($\partial_t \to \epsilon \partial_\tau$), results in

$$\left(\partial_\tau - \psi_{2y}^{(0)} \partial_x + \psi_{2x}^{(0)} \partial_y\right)\left(q_2^{(1)} - y\right) = 0. \tag{15}$$

WG89 recognised that equation (15) is simply a passive tracer advection equation, since the spatial structure of the streamfunction of the advecting velocity $\psi_2^{(0)}$ is known from the leading order solution (11). The "passive tracer" $Q = q_2^{(1)} - y$ is simply the leading order total PV in the lower layer. PV is of course an active tracer in general, in the sense

that it instantaneously determines the flow through PV inversion, but Q is passively advected in equation (15) because the flow in the lower layer *at leading order* is determined entirely by $q_1^{(0)}$, the leading order perturbation PV in the upper layer. Equation (15) can be further simplified into an passive tracer advection equation in a *steady* velocity field by first recognising that, because equation (15) is linear in $\psi_2^{(0)}$, the complex amplitude $A(\tau)$ in (11) can be set to be real without loss of generality, hence $|A(\tau)|$ is used hereafter. Second, the change of variables

$$\eta = \gamma_m \int_0^\tau |A(\tilde{\tau})| \, \mathrm{d}\tilde{\tau} \tag{16}$$

can be made, resulting in

$$\left(\partial_\eta - \Psi_y \partial_x + \Psi_x \partial_y\right) Q = 0, \quad \text{where } \Psi(x, y) = \cos(k_m x) \, \cos(\pi y / W). \tag{17}$$

The initial condition for (17) is simply $Q(x, y, 0) = -y$ in the case of the infinitesimal noise lifecycle described above. WG89's solution of (17), presented in Appendix B, is

$$Q(x, y, \eta) = -\frac{W}{\pi} \sin^{-1}\left[\frac{\sin(\pi y/W)\,\mathrm{cn}(\tilde{\eta}|m)\,\mathrm{dn}(\tilde{\eta}|m) + \sin(k_m x)\,\cos^2(\pi y/W)\,\mathrm{sn}(\tilde{\eta}|m)}{1 - \sin^2(\pi y/W)\,\mathrm{sn}^2(\tilde{\eta}|m)}\right], \tag{18}$$

where $\tilde{\eta} = k_m \pi \eta / W$, $m(x, y) = 1 - \cos^2(k_m x)\cos^2(\pi y/W)$, and $\mathrm{sn}(\cdot|\cdot)$, $\mathrm{cn}(\cdot|\cdot)$ and $\mathrm{dn}(\cdot|\cdot)$ are Jacobi elliptic functions in standard notation. The solution (18) is shown in figures 2(a–e) at re-scaled times $\eta = 0$, 0.79, 5.55, 10 and $15\, W/\pi k_m$, showing the development of the lower layer critical layer. The lower layer PV field is seen to wrap up within each circulation cell, and there is consequently a cascade of enstrophy within the lower layer to increasingly small scales.

The result (18) can be used to evaluate the integral in (14), since $q_2^{(1)} = y + Q$, to obtain an expression for the wave amplitude $|A(\tau)|$. The integral does not obviously lend itself to analytical evaluation, but can be written in a form suitable for numerical quadrature using the coordinate transformation described in Appendix B. Substituting (18) in (14), the WGP solution is found to be

$$|A(\tau)|^2 = W^2\left[\frac{2}{3} - \frac{16}{\pi^4}\, I\left(\frac{k_m \pi}{W}\eta\right)\right], \tag{19}$$

where $I(z)$ denotes the single parameter family of definite integrals

$$I(z) = \int_0^1 \int_0^{\mathrm{K}(m)} \frac{\sin^{-1}\left(m^{1/2}\mathrm{sn}(\alpha - z|m)\right) \sin^{-1}\left(m^{1/2}\mathrm{sn}(\alpha|m)\right)}{(1-m)^{1/2}} \, \mathrm{d}\alpha \, \mathrm{d}m.$$

where $\mathrm{K}(m)$ is the complete elliptic integral of the first kind. The function $I(z)$ has the following properties:

- $I(0) = \pi^4/24$, meaning that $\eta = |A(\tau)| = 0$ is a solution of (19), corresponding to the absence of a perturbation to the unstable flow.
- $I(z) \to 0$ as $z \to \infty$, meaning that the long time solution of (19), corresponding to the completely wrapped-up, or coarse-grain homogenized lower layer PV, is $|A|^2 \to |A|^2_{\mathrm{eq}} = 2W^2/3$.

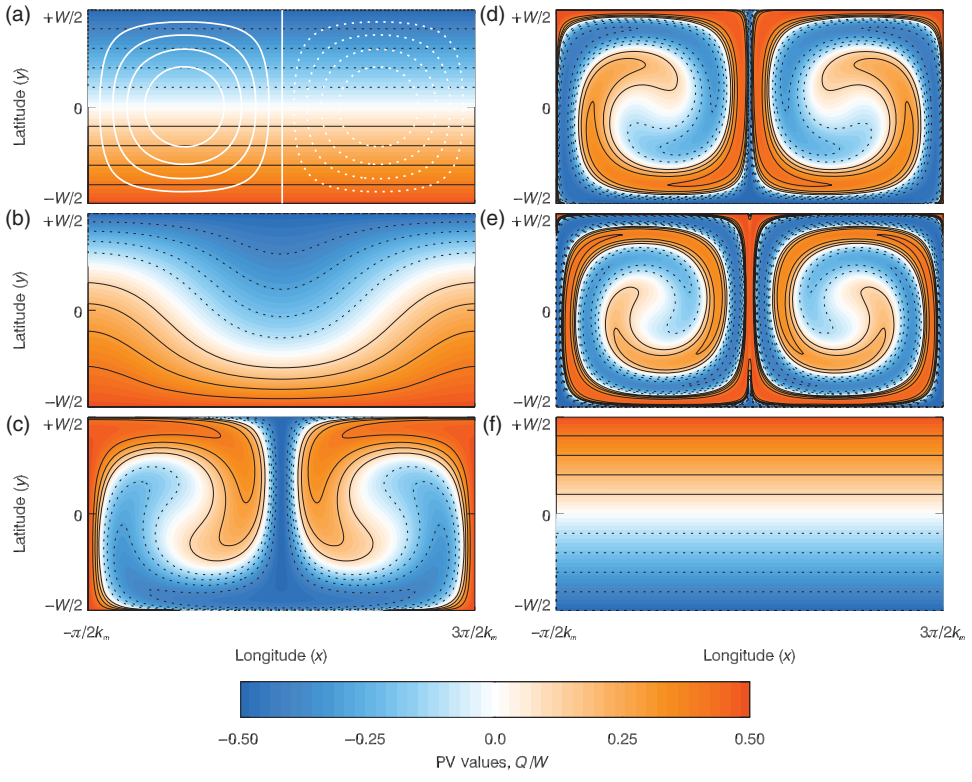

Figure 2. Snapshots of total lower layer PV ($Q(x, y, \eta)/W$) in the WGP solution (equation (18)) at scaled times (a–e) $\eta = 0$, 0.79, 5.55, 10 and $15W/k_m\pi$. The contour interval is 0.1. The advecting streamfunction $\psi_2^{(0)}$ is contoured in white in panel (a), with solid contours for the anti-cyclonic (clockwise) cell and dotted for the cyclonic (anti-clockwise). Its structure but not its magnitude is invariant in time, hence no fixed contour interval applies. The final panel (f) shows the "rearranged" PV field used for the WGP pseudomomentum bound (equation (21)).

- $I(z)$ decreases monotonically until its first local minimum at $z_m \approx 5.55$, which is also its global minimum. There $I(z_m) \approx -2.257$. The maximum amplitude attained is therefore $|A|^2_{\max} \approx 1.04W^2$. The lower layer Kelvin's impulse and upper layer wave amplitude are therefore both maximized at $\eta = 5.55W/\pi k_m$, and the lower layer PV at this time is shown in figure 2(c), which can be contrasted with the "perfect" rearrangement of lower layer PV in figure 2(f) to be discussed further below.

It should be emphasised that the solution (19) for $|A(\tau)|$ is implicit, as $|A(\tau)|$ is related to $\eta(\tau)$ through (16). The solution can be made explicit by noting that $|A(\tau)| = \gamma_m^{-1} \mathrm{d}\eta/\mathrm{d}\tau$, which can be used to rewrite (19) as

$$\tau = \frac{1}{\gamma_m W} \int_{\eta_0}^{\eta} \left[\frac{2}{3} - \frac{16}{\pi^4} I\left(\frac{k_m \pi}{W} \bar{\eta} \right) \right]^{-1/2} \mathrm{d}\bar{\eta}. \tag{20}$$

The constant η_0 is determined by the fact that, ultimately, a value must be ascribed to the amplitude of the infinitesimal wave in the initial conditions. Provided η_0 is chosen within a range that is sufficiently small, changes in η_0 correspond only to changes in the

time of the onset of the nonlinear part of the solution, which remains otherwise unaltered. The relationship (20) can be inverted numerically to give $\eta(\tau)$, which can in turn be differentiated numerically to obtain $|A(\tau)|$ explicitly. Further discussion of the inversion of the implicit form of the solution is given in WG89.

3.2. *The Held–Shepherd pseudomomentum bound on wave amplitude*

The derivation of the WGP solution given above is intimately related to upper bounds on wave amplitude that can be obtained using the methods of Arnol'd. For the situation considered here, the relevant bound is given by Shepherd (1988) but is attributed there to I.M. Held, hence it will be referred to as the Held–Shepherd bound here. Here, a brief and elementary derivation of the Held–Shepherd bound will be given, which bypasses much of the mathematical machinery introduced by Shepherd.† Before commencing, it is worth noting that in the WGP governing equation (14) which describes weakly supercritical flow, the wave amplitude is entirely determined by Kelvin's impulse in the lower layer. The lower layer Kelvin's impulse is obviously bounded above by the "rearranged" field shown in figure 2(f) in which $q_2^{(1)} = Q + y = 2y$. The resulting bound from (14) is

$$|A(\tau)|^2 = \frac{8}{\mathrm{LW}} \int_{\mathcal{D}} y q_2^{(1)} \, \mathrm{d}\boldsymbol{x} \leq \frac{8}{\mathrm{LW}} \int_{\mathcal{D}} 2y^2 \, \mathrm{d}\boldsymbol{x} = \frac{4W^2}{3}. \tag{21}$$

The WGP maximum wave amplitude $|A|_{\max}$ calculated above is therefore approximately 88% of the maximum attainable under the bound (21).

The Held–Shepherd bound can be obtained by extending essentially the same idea to the case of finite criticality. The initial aim is to obtain a bound on the perturbation enstrophy

$$Z' = Z_1' + Z_2' = \tfrac{1}{2} \int_{\mathcal{D}} (q_1')^2 + (q_2')^2 \, \mathrm{d}\boldsymbol{x}, \tag{22}$$

from which a bound on upper layer wave amplitude follows straightforwardly. Here q_1' denotes the non-zonal part of q_1 (i.e. $q_1' = q_1 - \bar{q}_1$ where the overbar denotes a zonal mean).

Inequalities for the perturbation enstrophy are constructed as follows:

$$\begin{aligned}
Z' &\leq \tfrac{1}{2} \int_{\mathcal{D}} (q_1')^2 + \lambda (q_2')^2 \, \mathrm{d}\boldsymbol{x}, && \text{for any } \lambda \geq 1 \\
&\leq \tfrac{1}{2} \int_{\mathcal{D}} (q_1 - \mu y)^2 + \lambda \Big(q_2 - \frac{\mu}{\lambda} y \Big)^2 \, \mathrm{d}\boldsymbol{x}, && \text{for any } \mu \in R \\
&= Z_1 + \lambda Z_2 - \mu M + \frac{\mathrm{LW}^3}{24} \frac{\mu^2(\lambda + 1)}{\lambda}, \\
&= \frac{\mathrm{LW}^3}{24} \left(\big(\beta + \tfrac{1}{2}\big)^2 + \lambda \big(\beta - \tfrac{1}{2}\big)^2 - 4\mu\beta + \frac{\mu^2(\lambda + 1)}{\lambda} \right),
\end{aligned} \tag{23}$$

†Shepherd's method is of course much more general and more widely applicable. It is the simplicity of the uniform flow initial conditions in Phillips model that permits the simpler derivation given here, and allows the relationship with the WGP solution to be clarified.

using the initial values for Z_i and M given in (7a–c) and (8). The above bound holds for any $(\lambda, \mu) \in [1, \infty) \times \mathbb{R}$. The tightest bound will either be at the critical point (λ_c, μ_c) of the function

$$g(\lambda, \mu) = \left(\beta + \tfrac{1}{2}\right)^2 + \lambda\left(\beta - \tfrac{1}{2}\right)^2 - 4\mu\beta + \frac{\mu^2(\lambda + 1)}{\lambda},$$

which is located at

$$(\lambda_c, \mu_c) = \left(\frac{3\beta - \frac{1}{2}}{\frac{1}{2} - \beta}, 3\beta - \tfrac{1}{2}\right),$$

or will be located along the line $\lambda = 1$ at $(\lambda, \mu) = (1, \beta)$. A straightforward calculation reveals the former case holds for $\frac{1}{4} \le \beta < \frac{1}{2}$ and the latter for $0 < \beta < \frac{1}{4}$. The Held–Shepherd bound is thus found to be

$$Z' \le \frac{\mathrm{LW}^3}{48} \begin{cases} 16\beta(\frac{1}{2} - \beta) & \frac{1}{4} \le \beta \le \frac{1}{2}, \\ 1 & 0 < \beta < \frac{1}{4}. \end{cases} \tag{24}$$

Appendix A discusses the change in notation compared to Shepherd's work.

A bound on wave amplitude at finite criticality is obtained by applying the same analysis to the upper layer perturbation enstrophy Z_1'. The only change in the analysis is that the range of possible λ is extended to $[0, \infty)$, with the tightest bound for $\beta < 1/6$ coming for $(\lambda, \mu) = (0, 0)$. The result is

$$Z_1' \le \frac{\mathrm{LW}^3}{48} \begin{cases} 16\beta(\frac{1}{2} - \beta) & \frac{1}{6} \le \beta \le \frac{1}{2}, \\ 2(\beta + \frac{1}{2})^2 & 0 < \beta < \frac{1}{6}. \end{cases} \tag{25}$$

The bound for $\beta < 1/6$ is simply the total enstrophy in the upper layer i.e. Z_1 above. The result (25) is converted to a wave amplitude bound by noting that the complex amplitude A_1^f of the fundamental wave in the upper layer, given by (9) above, satisfies the inequality (cf. Bessel's inequality for Fourier series)

$$|A_1^f|^2 \le \frac{8Z_1'}{\mathrm{LW}} \le \frac{W^2}{6} \begin{cases} 16\beta(\frac{1}{2} - \beta) & \frac{1}{6} \le \beta \le \frac{1}{2}, \\ 2(\beta + \frac{1}{2})^2 & 0 < \beta < \frac{1}{6}. \end{cases} \tag{26}$$

In the limit $\epsilon \to 0$ ($\beta \to \frac{1}{2}$), in which the complex amplitude A_1^f can be identified with $-\epsilon A$ in the WGP solution, it is clear that (26) reduces to the WGP result (21).

A bound on the lower layer PV perturbation amplitude $|A_2^f|$, that will be of use for the interpretation of numerical results below, can be obtained by similar means. Using the trivial bound on the lower layer perturbation enstrophy from (8),

$$Z_2' \le Z_2 = Z_2(0) = \frac{\mathrm{LW}^3}{24}(\tfrac{1}{2} - \beta)^2,$$

the bound can be obtained as

$$|A_2^f|^2 \le \frac{8Z_2'}{\mathrm{LW}} \le \frac{W^2}{3}(\tfrac{1}{2} - \beta)^2. \tag{27}$$

3.3. *Pseudoenergy bounds on wave energy*

A similar approach can be taken to recover and improve upon pseudoenergy bounds given by Shepherd (1993). Shepherd's objective was to a formulate a bound on the perturbation energy

$$E' = \tfrac{1}{2}\int_{\mathcal{D}} |\nabla\psi_1'|^2 + |\nabla\psi_2'|^2 + \tfrac{1}{2}(\psi_1' - \psi_2')^2 \,\mathrm{d}\boldsymbol{x}.$$

Here, a starting point is to introduce a "basic state" streamfunction $\Psi_i(y)$ $(i=1,2)$, which from the symmetry in the problem is assumed to be an odd function in y, and satisfies boundary conditions

$$\Psi_i = \mp\tfrac{1}{2}\alpha_i W \quad \text{on } y = \pm\tfrac{1}{2}W,$$

for some undetermined constants α_i. Note that α_i corresponds to the cross-channel average of the associated basic zonal flow $(-\Psi_{iy})$ in layer i.

The basic streamfunction Ψ_i can be used to formulate the following inequality, using integration by parts,

$$\begin{aligned}
E' &= \tfrac{1}{2}\int_{\mathcal{D}} |\nabla\psi_1'|^2 + |\nabla\psi_2'|^2 + \tfrac{1}{2}(\psi_1' - \psi_2')^2 \,\mathrm{d}\boldsymbol{x},\\
&\le \tfrac{1}{2}\int_{\mathcal{D}} |\nabla(\psi_1 - \Psi_1)|^2 + |\nabla(\psi_2 - \Psi_2)|^2 + \tfrac{1}{2}((\psi_1 - \psi_2) - (\Psi_1 - \Psi_2))^2 \,\mathrm{d}\boldsymbol{x}\\
&= E - \int_{\mathcal{D}} \nabla\psi_1\cdot\nabla\Psi_1 + \nabla\psi_2\cdot\nabla\Psi_2 + \tfrac{1}{2}(\psi_1 - \psi_2)(\Psi_1 - \Psi_2)\mathrm{d}\boldsymbol{x}\\
&\quad + \tfrac{1}{2}\int_{\mathcal{D}} (\Psi_{1y})^2 + (\Psi_{2y})^2 + \tfrac{1}{2}(\Psi_1 - \Psi_2)^2 \,\mathrm{d}\boldsymbol{x}\\
&= E + \int_{\mathcal{D}} (\Psi_1 q_1 + \Psi_2 q_2)\mathrm{d}\boldsymbol{x} - \alpha_1 \mathrm{LW} + \tfrac{1}{2}\int_{\mathcal{D}} (\Psi_{1y})^2 + (\Psi_{2y})^2\\
&\quad + \tfrac{1}{2}(\Psi_1 - \Psi_2)^2 - 2\beta y(\Psi_1 + \Psi_2)\mathrm{d}\boldsymbol{x}.
\end{aligned} \tag{28}$$

Note that all of the terms in the final line of (28) are easily bounded except for the first integral. A similar approach can be used to bound $\nu Z'$ (i.e. a constant $\nu > 0$ times the perturbation enstrophy)

$$\begin{aligned}
\nu Z' &= \tfrac{1}{2}\nu\int_{\mathcal{D}} (q_1')^2 + (q_2')^2 \,\mathrm{d}\boldsymbol{x}\\
&\le \tfrac{1}{2}\nu\int_{\mathcal{D}} (q_1')^2 + \lambda(q_2')^2 \,\mathrm{d}\boldsymbol{x} \qquad \text{for } \lambda \ge 1\\
&\le \tfrac{1}{2}\nu\int_{\mathcal{D}} \left(q_1 - \frac{1}{\nu}(\Psi_1 + \mu y)\right)^2 + \lambda\left(q_2 - \frac{1}{\lambda\nu}(\Psi_2 + \mu y)\right)^2 \mathrm{d}\boldsymbol{x}\\
&= \nu Z_1 + \nu\lambda Z_2 - \mu M - \int_{\mathcal{D}} (\Psi_1 q_1 + \Psi_2 q_2)\mathrm{d}\boldsymbol{x} + \frac{1}{2\nu}\int_{\mathcal{D}} (\Psi_1 + \mu y)^2 + \frac{1}{\lambda}(\Psi_2 + \mu y)^2 \,\mathrm{d}\boldsymbol{x}.
\end{aligned} \tag{29}$$

Summing the inequalities for E' and $\nu Z'$, the ''difficult-to-bound'' integrals cancel giving

$$E' + \nu Z' \leq E + \nu Z_1 + \nu\lambda Z_2 - \mu M - \alpha_1 \mathrm{LW} + \tfrac{1}{2}\int_{\mathcal{D}} (\Psi_{1y})^2 + (\Psi_{2y})^2 + \tfrac{1}{2}(\Psi_1 - \Psi_2)^2 - 2\beta y(\Psi_1 + \Psi_2) + \frac{1}{\nu}(\Psi_1 + \mu y)^2 + \frac{1}{\lambda\nu}(\Psi_2 + \mu y)^2 \,\mathrm{d}\boldsymbol{x}, \quad (30)$$

where, as before, M, E, Z_1 and Z_2 are determined by their initial values given in (7a–c) and (8).

Shepherd's bound follows from choosing Ψ_i to be the streamfunction of a uniform flow, namely

$$\Psi_1 = -\alpha_1 y, \quad \Psi_2 = -\alpha_2 y.$$

The integral in (30) is now straightforward to evaluate, giving

$$E' + \nu Z' \leq \frac{\mathrm{LW}}{2}\left((1-\alpha_1)^2 + \alpha_2^2\right) + \frac{\mathrm{LW}^3}{48}\Big[1 + 2\nu(\beta + \tfrac{1}{2})^2 + 2\lambda\nu(\beta - \tfrac{1}{2})^2 + 4\beta(\alpha_1 + \alpha_2 - 2\mu) + 2(\alpha_1 - \alpha_2)^2 + \frac{4}{\nu}(\alpha_1 - \mu)^2 + \frac{4}{\lambda\nu}(\alpha_2 - \mu)^2\Big]. \quad (31)$$

The bound can now be minimized with respect to the free parameters $(\alpha_1, \alpha_2, \mu, \nu, \lambda)$ over the domain $\mathbb{R}\times\mathbb{R}\times\mathbb{R}\times(0,\infty)\times[1,\infty)$. Equation (31) is quadratic in $(\alpha_1, \alpha_2, \mu)$, consequently the optimal bound with respect to these parameters is found by solution of a linear system to occur at the critical values

$$\alpha_{1,2\,c} = \frac{1}{2} \pm \frac{6 - \beta W^2 + \lambda(6 + \beta W^2)}{2W^2 + \nu(1+\lambda)(12 + W^2)}\ \nu,$$

$$\mu_c = \frac{2W^2 + 4\nu^2\lambda\beta(12 + W^2) + \nu\left((2\beta+1)W^2 + \lambda(24 + W^2 + 2\beta W^2)\right)}{2(2W^2 + \nu(1+\lambda)(12+W^2))}.$$

Inserting these into (31) results in

$$E' + \nu Z' \leq \frac{\mathrm{LW}^3}{24}\frac{\left(1 + \nu(\beta + \frac{1}{2}) - \nu\lambda(\beta - \frac{1}{2})\right)^2(12 + W^2)}{2W^2 + \nu(1+\lambda)(12+W^2)}.$$

The critical point leading to the minimum of the bound, viewed as a function of (λ, ν), can be shown by direct differentiation to lie on the curve

$$\lambda_c(\nu) = \frac{24 + (8\beta - 2)W^2 + \nu(6\beta - 1)(W^2 + 12)}{2\nu(\frac{1}{2} - \beta)(W^2 + 12)},$$

which when inserted into the bound gives

$$E' + \nu Z' \leq \frac{\mathrm{LW}^3}{6}(\tfrac{1}{2} - \beta)\left(1 - \frac{2(\frac{1}{2} - \beta)W^2}{W^2 + 12} + 2\beta\nu\right). \quad (32)$$

However, the constraint $\lambda \geq 1$ means that the above critical point provides the optimal bound for E' in the limit $\nu \to 0$ only under the condition that

$$\beta \geq \frac{1}{4} - \frac{3}{W^2}.$$

Otherwise, the optimal bound is at $(\lambda, \mu) = (1, 0)$ giving

$$E' \leq \frac{\mathrm{LW}}{48}(W^2 + 12).$$

Combining these results gives the desired bound on E'

$$E' \leq \frac{\mathrm{LW}^3}{6} \begin{cases} \left(\frac{1}{2} - \beta\right)\left(1 - \dfrac{2W^2}{W^2 + 12}\left(\frac{1}{2} - \beta\right)\right) & \dfrac{1}{4} - \dfrac{3}{W^2} \leq \beta < \dfrac{1}{2}, \\ \dfrac{1}{8}\left(1 + \dfrac{12}{W^2}\right) & 0 < \beta < \dfrac{1}{4} - \dfrac{3}{W^2}. \end{cases} \tag{33}$$

In the appendix, the bound (33) is compared with the corresponding bound in Shepherd (1993, see his (8.2)). In the notation of this work, Shepherd's bound is

$$E' \leq \frac{\mathrm{LW}^3}{6} \begin{cases} \left(\frac{1}{2} - \beta\right)\left(1 - \dfrac{48 - 2W^2}{W^2}\left(\frac{1}{2} - \beta\right)\right), \\ \dfrac{1}{8}\left(1 + \dfrac{12}{W^2}\right). \end{cases} \tag{34}$$

It is clear that (33) improves upon (34).

3.4. *Towards an optimal pseudoenergy bound on wave energy*

The bounds above can be improved upon by relaxing the constraint that Ψ_i corresponds to a uniform flow. For fixed $(\alpha_1, \alpha_2, \mu, \nu, \lambda)$, finding Ψ_i to minimize the integral expression in (30) is a straightforward calculus of variations problem. Ψ_i must satisfy the Euler–Lagrange equations

$$\begin{pmatrix} \Psi_1 \\ \Psi_2 \end{pmatrix}_{yy} + \begin{pmatrix} -\frac{1}{2} - (1/\nu) & \frac{1}{2} \\ \frac{1}{2} & -\frac{1}{2} - (1/\lambda\nu) \end{pmatrix} \begin{pmatrix} \Psi_1 \\ \Psi_2 \end{pmatrix} = \begin{pmatrix} \left((\mu/\nu) - \beta\right) y \\ \left((\mu/\lambda\nu) - \beta\right) y \end{pmatrix}, \tag{35}$$

with $\Psi_i = \mp\frac{1}{2} W\alpha_i$ on $y = \pm\frac{1}{2} W$. In order to make the problem (35) more manageable an assumption can be made at this stage that the underlying structure of the optimisation problem with respect to the free parameters $(\alpha_1, \alpha_2, \mu, \nu, \lambda)$ remains similar to that in the uniform flow case above. In the uniform flow case, the tightest bound was found by taking the distinguished limit $\nu \to 0$, $\lambda \to \infty$, $\nu\lambda \to q$ (constant). The same distinguished limit can be taken before trying to solve (35).

In this distinguished limit the equation for Ψ_1 reduces to

$$\Psi_1(y) = -\mu y, \tag{36}$$

where the additional condition $\alpha_1 = \mu$ is enforced by the need to suppress thin boundary layers at the sidewalls, which can only contribute positively to the integral in (30). The Ψ_2 equation becomes

$$\Psi_{2yy} - \left(\frac{1}{2} + \frac{1}{q}\right)\Psi_2 = \left(\mu\left(\frac{1}{2} + \frac{1}{q}\right) - \beta\right) y \quad \text{with } \Psi_2 = \mp\tfrac{1}{2} W\alpha_2 \quad \text{on } y = \pm\tfrac{1}{2} W, \tag{37}$$

which has solution given by

$$\Psi_2(y) = \frac{2q\beta - (q+2)\mu}{q+2}\, y - \frac{(2q\beta + (\alpha_2 - \mu)(q+2))W}{2(q+2)\sinh\left(\sqrt{\frac{1}{2}+\frac{1}{q}}\,\frac{W}{2}\right)}\sinh\left(\sqrt{\tfrac{1}{2}+\tfrac{1}{q}}\,y\right). \tag{38}$$

The solutions $\{\Psi_1(y), \Psi_2(y)\}$ of the Euler–Lagrange equations given by (36) and (38) can be inserted into the expression (30), and the resulting expression minimized over the remaining parameters (α_2, μ, q). Some details of the calculation are given in the appendix. The result is

$$E' \leq \mathrm{LW}\ \mathrm{Min}_{q>0}\{\mathcal{G}(q, \beta, W)\}, \tag{39}$$

where

$$\mathcal{G}(q, \beta, W) = \frac{\left(1 + (\tfrac{1}{2} - \beta)q\right)^2\left((48 + (q+2)W^2)\tanh\left(\sqrt{\tfrac{1}{2}+\tfrac{1}{q}}\,\tfrac{W}{2}\right) - \sqrt{\tfrac{1}{2}+\tfrac{1}{q}}W(24 + (q+2)W^2)\right)}{24(q+2)^2\left(\tanh\left(\sqrt{\tfrac{1}{2}+\tfrac{1}{q}}\,\tfrac{W}{2}\right) - W\sqrt{\tfrac{1}{2}+\tfrac{1}{q}}\right)}.$$

Numerical calculation of the bound (39) shows that it is tighter than (33) throughout the relevant parameter space $(\beta, W) \in [0, 1/2] \times [2^{1/4}\pi, \infty)$. Disappointingly, the improvement over (33) is only a few per cent at best, indicating that (33) is sufficiently accurate for practical calculations.

The bound (39) can be accurately estimated for $\beta > 1/4 - 3/W^2$, i.e. where (33) is given by the upper solution, using the estimate $q_* \approx 1/(\frac{1}{2} - \beta) - J(W)$ for the location q_* of the minimum of $\mathcal{G}(q, \beta, W)$. Here

$$J(W) = \frac{4\sqrt{2}W(W^2 - 12) - 8(W^2 - 24)\tanh(W/2\sqrt{2})}{W^2(\sqrt{2}W - 2\tanh(W/2\sqrt{2}))}.$$

The result is the following explicit bound, which is very close to the exact result (39),

$$E' \leq \mathrm{LW}\,\mathcal{G}\left((\tfrac{1}{2} - \beta)^{-1} - J(W), \beta, W\right). \tag{40}$$

The bounds (33), (39) and (40) all have the form $(\mathrm{LW}^3/6)\epsilon^2 + \mathrm{O}(\epsilon^3)$, i.e. they are identical in the limit $\epsilon = (\frac{1}{2} - \beta)^{1/2} \to 0$.

4. Comparison with fully nonlinear behaviour

Next the numerical model described in section 2.2 will be used to address the questions highlighted in section 1, using a suite of simulations spanning the region of (β, W) parameter space for which the flow is unstable. The focus will be on a set of experiments with channel width $W = 2^{3/4}\pi \approx 5.283$, a value that has physical significance since the fastest growing mode in the channel is then isotropic (i.e. $k_m = \pi/W = 2^{-3/4}$) in the weakly supercritical limit (in which $a_m = 2^{-1/4}$).

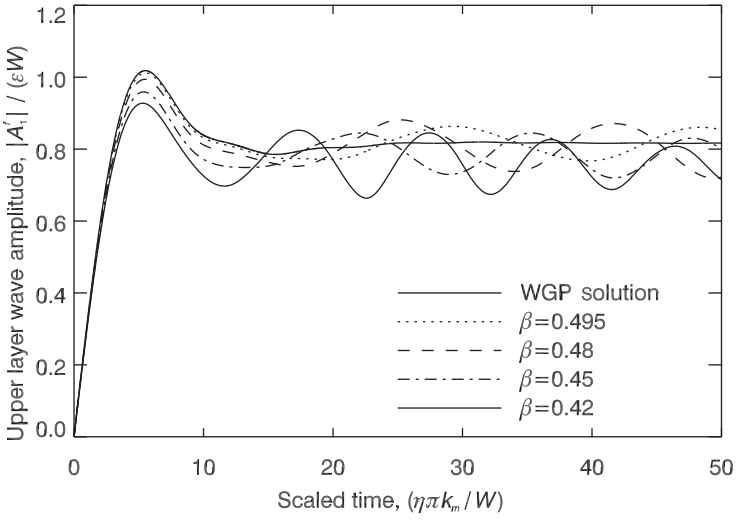

Figure 3. Evolution in scaled time (η) of the upper layer wave amplitude $|A_1^f|/\epsilon W$ for simulations with $W = 2^{3/4}\pi$ and $\beta = 0.495, 0.48, 0.45$ and 0.42 (broken curves), together with the WGP solution (solid curve).

4.1. *Is the WGP solution relevant at finite supercriticality?*

Figure 3 compares the evolution in η (scaled time) of the WGP wave amplitude $|A|/W$, given by equation (19), with the results of simulations of the fully nonlinear numerical model for criticalities in the range $\beta \in [0.42, 0.495]$. The quantity plotted from the simulations is the wave amplitude defined in equation (9), scaled as $|A_1^f|/\epsilon W$ to agree with WGP in the limit $\epsilon \to 0$. The scaled time η necessary to compare the solutions is obtained from the nondimensional time t in the simulations using (cf. equation (16))

$$\eta = \gamma_m \int_0^t |A_1^f(t')| \, \mathrm{d}t'.$$

For $\eta \lesssim 10W/k_m\pi$ the fully nonlinear results (dotted and dashed curves) appear to converge to the WGP solution (solid curve) as $\beta \to \frac{1}{2}$. Consequently, the maximum wave amplitude attained during the lifecycle is accurately predicted by WGP for low supercriticalities. For $\eta \gtrsim 10W/k_m\pi$, however, the WGP and fully nonlinear solutions diverge significantly, with the WGP solution approaching a constant amplitude ($|A|^2 = 2W^2/3$) relatively quickly, whereas the fully nonlinear solutions oscillate around this value. It is notable that as $\beta \to \frac{1}{2}$ the fully nonlinear solution diverges more slowly from WGP, and the period of the resulting oscillation grows longer. However, it is unclear whether or not, in the absence of numerical diffusion, the amplitude of the oscillation decreases as $\beta \to \frac{1}{2}$. The apparent decrease in oscillation amplitude seen in figure 3 (e.g. for the $\beta = 0.495$ simulation) could in fact be due to longer integration times, which scale as ϵ^{-1}, leading to an increase in the time-integrated effects of the numerical diffusion described in section 2.2. Recall that the period of the oscillation, as well as the early time behaviour of the solution, was shown to be insensitive to numerical resolution (and thus ν_q) in section 2.2.

The evolution of the lower layer PV holds the key to understanding the divergence between the fully nonlinear simulations and the WGP solution. Figure 4 shows the full

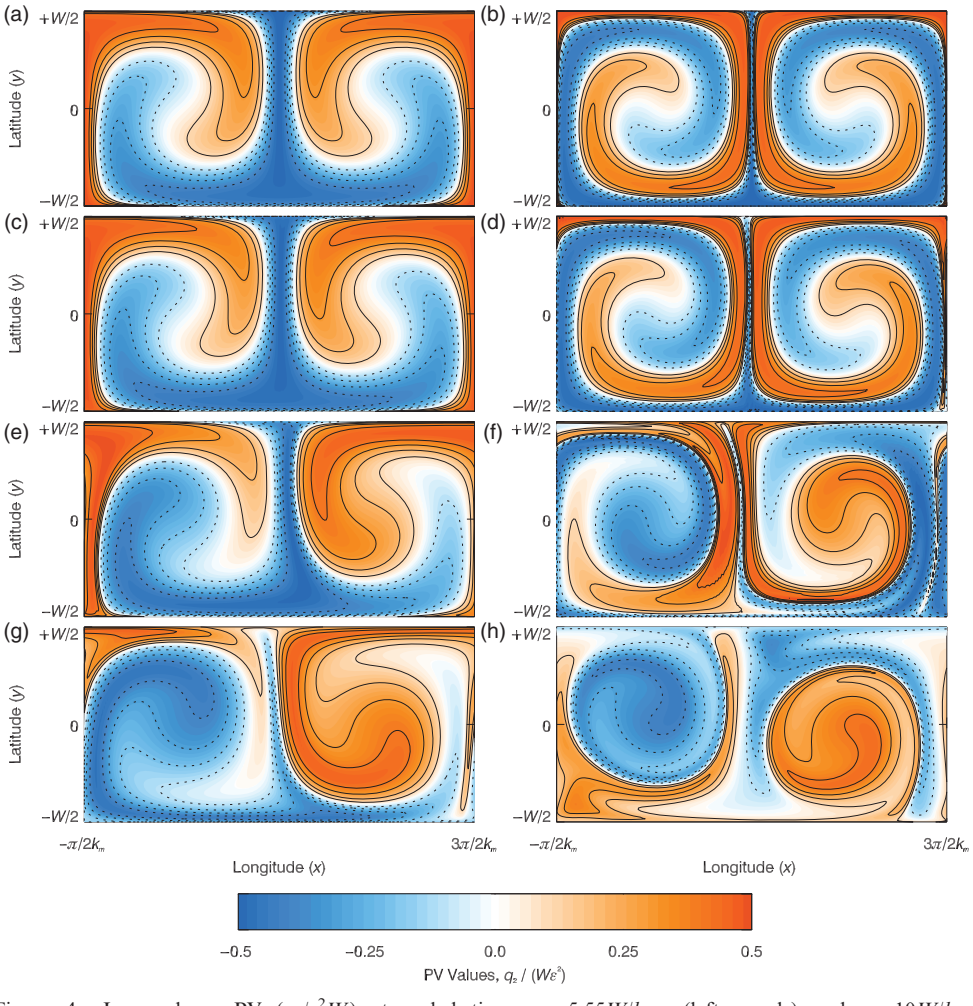

Figure 4. Lower layer PV ($q_2/\epsilon^2 W$) at scaled times $\eta = 5.55W/k_m\pi$ (left panels) and $\eta = 10W/k_m\pi$ (right panels), for simulations with $W = 2^{3/4}\pi$. (a, b) WGP solution. (c, d) $\beta = 0.495$. (e, f) $\beta = 0.4$. (g–h) $\beta = 0.2$. The contour interval is 0.1 and the zero contour is omitted.

(scaled) lower layer PV distribution $q_2/\epsilon^2 W$ at fixed (scaled) times $\eta = 5.55W/k_m\pi$ (left column) and $\eta = 10W/k_m\pi$ (right column) for simulations with $W = 2^{3/4}\pi$ and $\beta = 0.2$, 0.4 and 0.495 together with the corresponding WGP field Q/W given by (18) (top row).

The low supercriticality simulation ($\beta = 0.495$) reproduces the WGP solution fairly closely in both snapshots. Nevertheless, there is a slight asymmetry present between the two circulation cells, which are exactly (anti-)symmetric in the case of WGP. In the simulation, the cyclonic (anti-clockwise here) circulation cell entrains slightly more cyclonic PV (red) than anti-cyclonic (blue). The asymmetry is much more pronounced at higher supercriticalities. For $\beta = 0.40$ and 0.20, a vortex forms within each circulation cell, and by $\eta = 10W/k_m\pi$ these are positioned exactly in phase with the upper layer wave (not shown). Note that the sign of these vortices is such that the circulation within each cell is enhanced, i.e. there is a tendency towards barotropization in fully nonlinear

flows, as is observed in isotropic quasi-geostrophic two-layer turbulence (see, e.g. the discussion in Vallis 2006, sec. 9.2.3). The results show that the mechanism of equilibration changes as the supercriticality increases. In all cases equilibration is attained via the removal of the lower layer zonal mean PV gradient. In WGP and at low supercriticality, the lower layer PV gradient is removed by stirring and eventual (coarse-grain) homogenization of the entire lower layer PV field. At higher supercriticalities, by contrast, the lower layer PV rolls up into a train of opposite signed vortices, one pair per wavelength of the upper layer wave. The transition between the two behaviours is discussed and quantified further below.

Figure 5 shows snapshots of the lower layer PV for the WGP solution and the simulations with $\beta = 0.48$ and $W = 4, 2^{3/4}\pi$ and 10. It might be anticipated that at such a low supercriticality the dependence of the evolution on W would be weak, since the

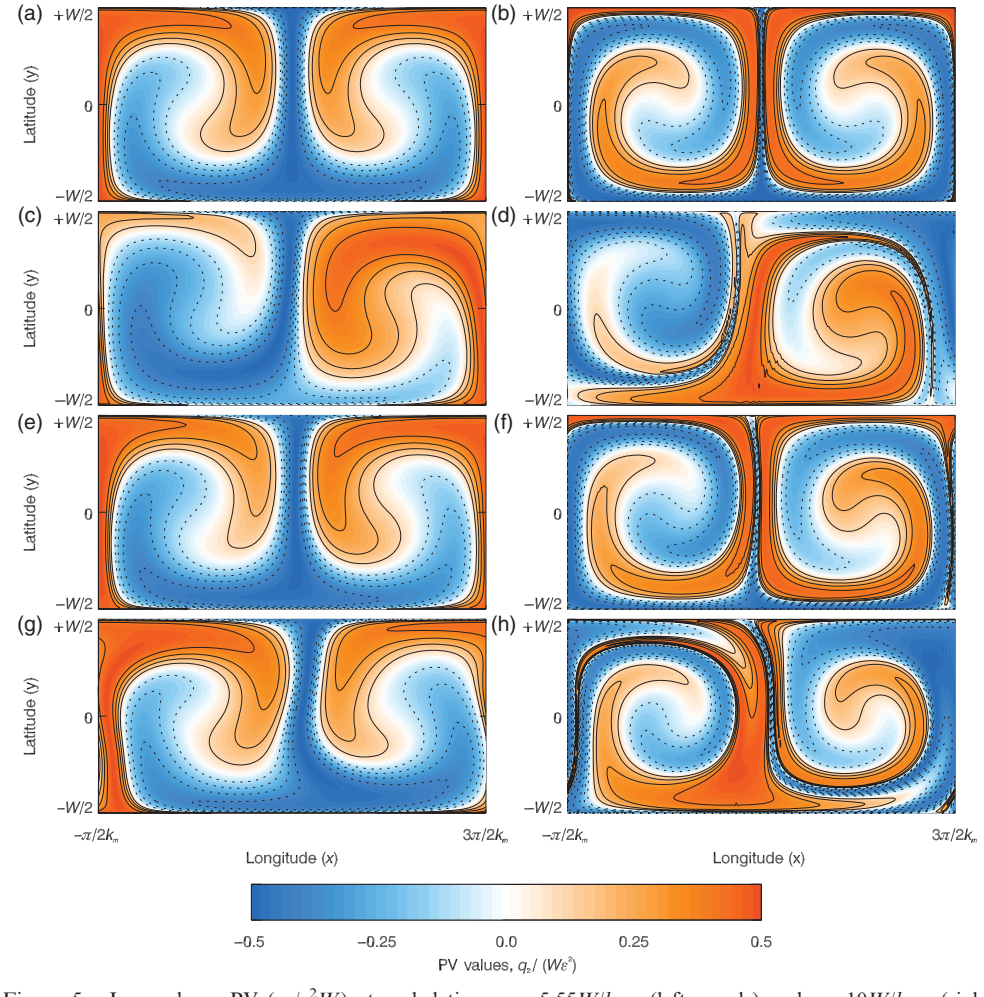

Figure 5. Lower layer PV ($q_2/\epsilon^2 W$) at scaled times $\eta = 5.55W/k_m\pi$ (left panels) and $\eta = 10W/k_m\pi$ (right panels), for (a, b) the WGP solution ($\beta \to \frac{1}{2}$, all W) and (c–h) simulations with $\beta = 0.48$. In (c, d) $W = 4$, (e, f) $W = 2^{3/4}\pi$ and (g, h) $W = 10$. The contour interval is 0.1 and the zero contour is omitted.

WGP solution and the Held–Shepherd bound (24) scale trivially with W (although the perturbation energy bound (33) does not). On the other hand, one might expect the WGP solution in very wide channels $W \gg 10$ to be subject to jet-forming secondary instabilities of the type discussed by Pedlosky (1975) and Berloff *et al*. (2009). Figure 5 shows, however, that even at moderate widths the differences between the simulation results and the WGP solution do depend significantly on W. To understand these differences, it is helpful to take note of the different aspect ratios (given by $k_m W/\pi$) of the circulation cells in the three simulations, which differ since the fastest growing normal mode emergent in each simulation has a quite different structure. For the simulations shown in figure 5 (with $\beta = 0.48$) these are $k_m W/\pi = 0.757$, 1.000, 1.893 for $W = 4$, $2^{3/4}\pi$, 10 respectively, indicating that the circulation cells in the $W = 4$ simulations are elongated in the zonal direction, those for $W = 2^{3/4}\pi$ are almost exactly isotropic, whereas those for $W = 10$ are elongated meridionally. The different aspect ratios of the circulation cells explain in part the different ways the simulations diverge from WGP. The $W = 2^{3/4}\pi$ simulation, with isotropic circulation cells, remains closest to WGP. For the $W = 4$ simulation, with zonally elongated circulation cells, the finite criticality asymmetry in the circulation branches is much more pronounced, and the vortex roll-up and barotropization resembles that seen in the $W = 2^{3/4}\pi$ isotropic simulations at much higher supercriticality (cf. figures 4(c) and (f)). The $W = 10$ simulation, with meridionally elongated circulation cells, by contrast exhibits a rather different asymmetry within each circulation cell. Within a circulation cell in figure 5(d), the north–south branches appear to be almost antisymmetric in x. However, the east-west branches are not quite antisymmetric in y, indicating that the asymmetry leading to the differences with WGP is rotated through $\pi/2$ compared to the other simulations. The asymmetry in this case does not lead to vortex roll-up and barotropization but rather, as seen in figure 5(h), a more complex route to stirring and coarse-grain homogenization of the lower layer PV. The finding that zonally elongated circulation cells tend to promote vortex roll-up and barotropization, while meridionally elongated cells promote homogenization, will be investigated further below.

The late time divergence between WGP and the simulations at low supercriticality, evident in figure 3, can be investigated further by means of the following diagnostics. A measure of difference between the lower layer PV in the simulations and the WGP solution is given by the error measure

$$\mathcal{E}(\eta) = \frac{1}{\mathrm{LW}^2} \left\| \epsilon^{-2} q_2 - Q \right\|_1 , \tag{41}$$

where the norm is the usual L^1-norm defined to be

$$\| \cdot \|_1 = \int_D | \cdot | \, \mathrm{d}\boldsymbol{x}.$$

The evolution of $\mathcal{E}(\eta)$ is plotted in figure 6 (left) for simulations with $W = 2^{3/4}\pi$ and $\beta = 0.495$, 0.48, 0.44 and 0.40. Clearly, $\mathcal{E}(\eta)$ grows more rapidly as the supercriticality increases, and at short times the growth is found to be quadratic in η (which corresponds to exponential growth in time t via equation 16).

Figure 6 (right) shows the dependence of the time $\eta_{0.025}$, defined to be the scaled time satisfying $\mathcal{E}(\eta_{0.025} k_m \pi/W) = 0.025$, on the supercriticality ϵ. It is clear from the slope of the fit in the log–log plot, which is almost exactly $-\frac{1}{2}$, that the simulations are diverging

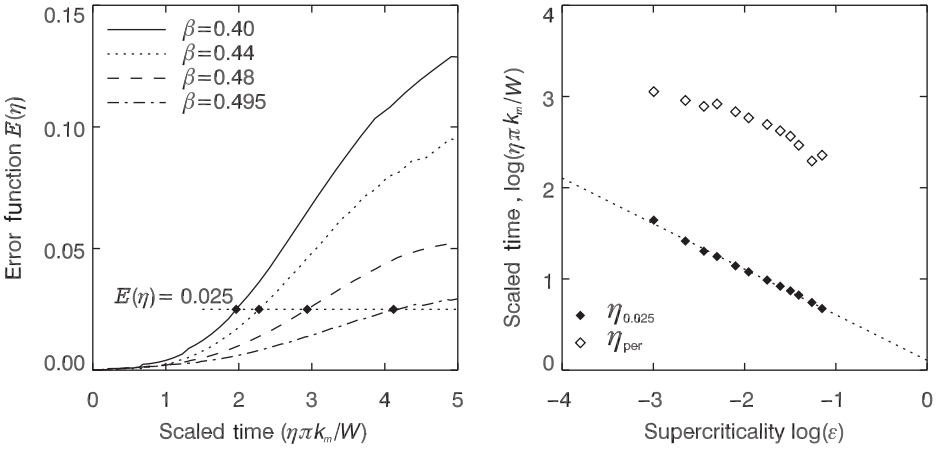

Figure 6. Left: Evolution of the error measure $\mathcal{E}(\eta)$ (defined by Equation 41) for inverse criticalities $\beta = 0.40$, 0.44, 0.48, 0.495. Right: Log–log plot of the growth rate of the error measure (determined from the scaled time $\eta_{0.025}$ defined in the text), and the period of the resulting oscillations η_{per}, as a function of the supercriticality ϵ.

from the WGP solution on a scaled timescale $\sim\epsilon^{-1/2}$ or a physical (i.e. variable t with units L_D/U) timescale $\sim\epsilon^{-3/2}$. The WGP solution develops on a physical timescale $\sim\epsilon^{-1}$, and is formally valid only up to times $\tau = \epsilon t = \mathrm{O}(1)$. The fact that the simulations diverge from WGP on a longer $\mathrm{O}(\epsilon^{-3/2})$ timescale is therefore not inconsistent with the nature of the multiple-scales method used to obtain WGP. Also shown in figure 6 (right) are estimates of the period η_{per} of the late-time oscillations apparent in figure 3, also plotted as a function of $\log \epsilon$. The period also seems to scale approximately with $\epsilon^{-1/2}$ in scaled time, or $\epsilon^{-3/2}$ in the original timescale.

4.2. *Assessment of pseudomomentum and pseudoenergy bounds*

A natural question to ask with regard to the pseudomomentum wave amplitude bounds (26) and (27), and the perturbation energy bound (39), concerns how closely they are attained in the simulations. The question is fundamental, as it relates to the question of the extent to which baroclinic flows are controlled by their known dynamical constraints, and therefore to the promise of predictive theories based on these (e.g. Esler 2008).

Figure 7(a) plots the maximum upper layer wave amplitude $|A_1^f|_{\max}/\epsilon W$ attained during the simulations (solid points), the corresponding equilibrated wave amplitude $|A_1^f|_{\mathrm{eq}}/\epsilon W$ (open points), the bound (26) (solid line), and the predictions of WGP (dashed lines) as a function of the inverse criticality β. Results for different channel widths W are plotted as different symbols. The corresponding lower layer results are given in figure 7(b), where the relevant bound is (27). Note that the WGP theory predicts that the equilibrated amplitude is zero in the lower layer.

Figure 7 confirms the success of the WGP predictions at small supercriticalities ($0.4 \sim \beta < 0.5$) although the theory is relatively inaccurate in the narrow channel case $W = 4$. At all criticalities the maximum amplitude attained follows the corresponding bound, and in the upper layer in particular it appears that a simple predictive model

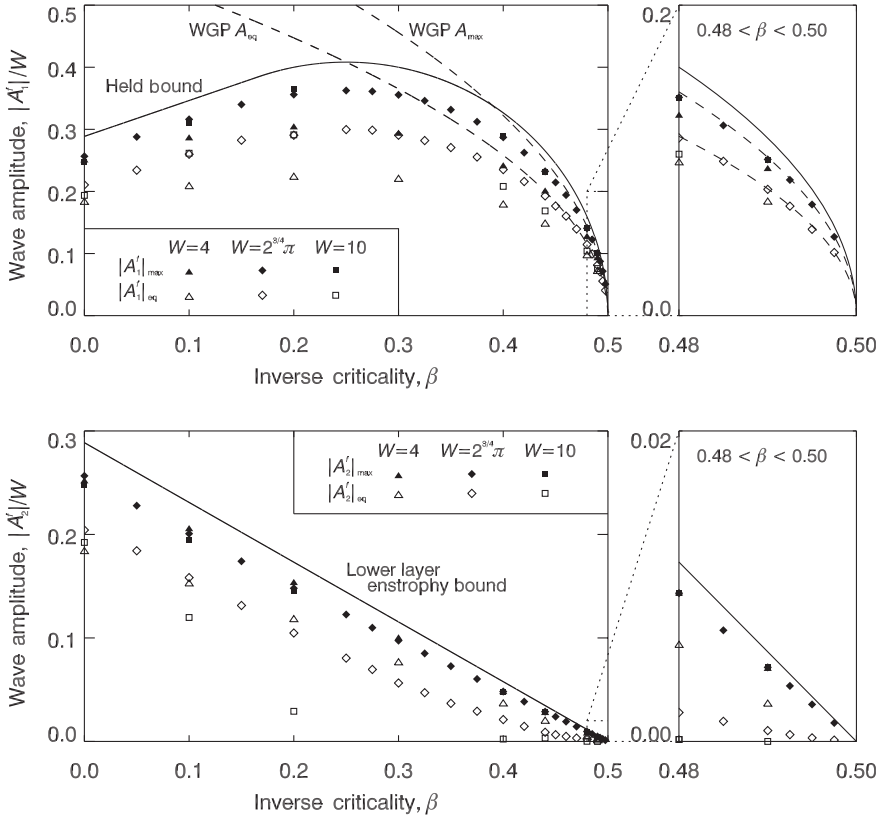

Figure 7. The maximum ($|A_i^f|_{\max}/W$, solid symbols) and equilibrated ($|A_i^f|_{eq}/W$, open symbols) wave amplitudes in the simulations as a function of inverse criticality β. The upper and lower panels correspond to the upper and lower layers ($i=1, 2$ respectively). The dashed lines in the upper panel correspond to the WGP predictions (derived from $|A|_{eq}$ and $|A|_{\max}$ defined in section 3). The solid lines are the amplitude bounds (upper panel: equation (26), lower panel: equation (27)) that follow from the Held–Shepherd bound. Different symbols correspond to different values of the width parameter W as indicated. The right-hand panels are blow-ups of the same plot at low supercriticality.

based on the wave amplitude attaining a fixed percentage (≈88%, the WGP value) of the bound (26) is reasonably accurate across much of parameter space, although less so when W is low.

The lower layer equilibrated amplitude results in figure 7(b) ($|A_2^f|_{eq}/\epsilon W$, open points) allow the different mechanisms of equilibration to be quantitatively identified. Lower layer PV homogenization and vortex roll-up can be easily distinguished in figure 7(b), since the lower layer wave amplitude must decay to zero if the PV field undergoes coarse-grain homogenization as in the WGP solution, whereas if the PV distribution rolls-up efficiently into coherent vortices the equilibrated amplitude will remain close to the bound (equation (26), solid curve). The results confirm the impression that PV homogenization occurs in the wide channel ($W=10$) simulations, with efficient vortex roll up occurring in the narrow channel ($W=4$) simulations, even at relatively low supercriticalities.

Figure 8 shows the maximum (solid points) and equilibrated (open points) perturbation energy (E'/LW^3) in the simulations, plotted as a function of inverse

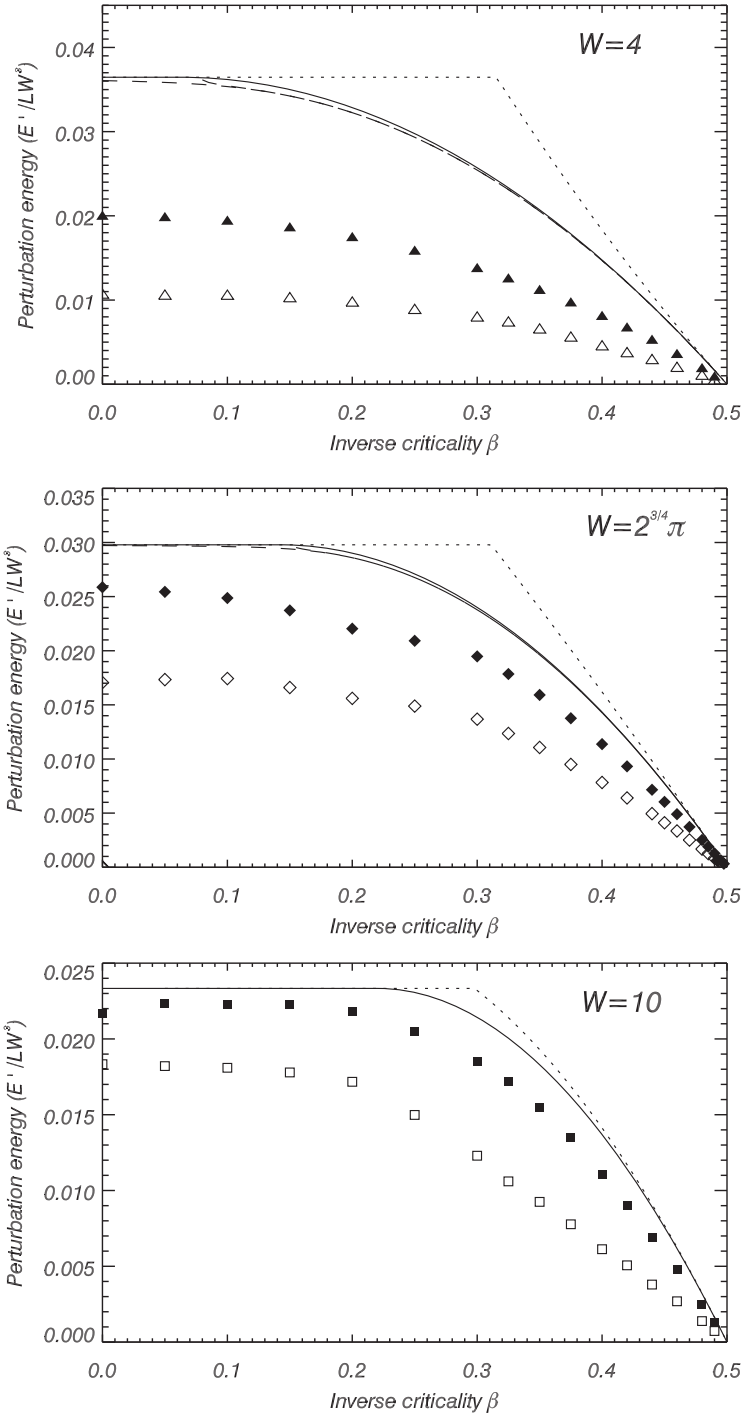

Figure 8. Maximum (solid symbols) and equilibrated (open symbols) perturbation energy (E'/LW^3) as a function of inverse criticality β in the simulations with $W=4$ (upper panel), $W=2^{3/4}\pi$ (middle panel) and $W=10$ (lower panel). The bounds of Shepherd (1993) equation (34) (dotted curve), equation (33) (solid curve) and equations (39) and (40) (dashed curves) are also plotted.

criticality β, together with the new bound (33), Shepherd's (1993) bound (34) and the variational bounds (39, 40). The latter are (almost) indistinguishable everywhere, and neither are plotted on the $W = 10$ panel because for large W they become indistinguishable from (33).

Figure 8 shows that in the wide channel ($W = 10$) simulation, the perturbation energy bounds are very nearly attained during the evolution of the lifecycles. For all of the narrow channel ($W = 4$) simulations, however, the perturbation energy attains only around 50% of the permissible value. The bounds (e.g. (33)) do not therefore appear to encode much useful information about how the lifecycle dynamics depend on W. The reason may be that the approach used in section 3 here is based on Arnol'd's first theorem. An approach that also exploits the second theorem (see, e.g. Mu *et al.* 1995) might allow some further improvement to the narrow channel bounds, since the second theorem utilizes the fact that the domain is finite. Such an improvement is beyond the scope of this work. The main utility of the perturbation energy bounds is therefore in the wide channel case, and the present simulations show that in this case nearly all available energy can be extracted from the mean flow once the inverse criticality satisfies $\beta \lesssim \frac{1}{4}$.

5. Conclusions

Here, nonlinear baroclinic equilibration in Phillips model has been investigated in detail. First, new, shorter derivations of the WGP analytical solution and Shepherd's pseudomomentum and pseudoenergy bounds on disturbance quantities have been presented. Second, a new formula has been found for the pseudoenergy bound, which has been further improved upon using a variational technique. Third, the new results have facilitated a comparison with fully nonlinear results from a high-resolution numerical model, and allow the questions posed in the introduction to be answered as follows:

- At low but finite supercriticalities ($\epsilon = (\frac{1}{2} - \beta)^{1/2} \ll 1$), the WGP solution can be realised numerically, but only for a finite time into the evolution of the lower layer critical layer. The early stages of lower layer critical layer development, similar to WGP, were found to be ubiquitous in our experiments at low supercriticalities. Formation of partial (i.e. localised in latitude) critical layers as reported by Gauthier (1990) was not found in any of our "infinitesimal noise" lifecycles, although was found in other (unreported) experiments with strong wavenumber discretization effects due to a finite channel length. The WGP predictions for peak wave amplitude are accurate at low supercriticality provided the channel width is not too small, and remain reasonable for $\beta \gtrsim 0.30$. At higher supercriticality (lower β), the WGP prediction is in conflict with the pseudomomentum bound, and cannot be accurate. The WGP solution gives reasonable predictions for equilibrated amplitudes, but at finite supercriticality the upper layer wave amplitude does not become steady as predicted.
- At finite supercriticality the simulations diverge from the WGP solution at long times. The divergence originates from an asymmetry in the entrainment of PV into the positive and negative circulation cells in the lower layer, which is not present in the symmetric WGP solution. As a consequence, the amplitude of the

fundamental oscillates about the steady-state value predicted by WGP, and the period of these oscillations scales as $\epsilon^{-3/2}$. There is little evidence that the divergence from WGP is due to barotropic instability arising from reversals of the zonal mean PV gradient within the lower layer, and therefore appears to be unrelated to the instability of the Stewartson–Warn–Warn Rossby wave critical layer (see, e.g. Haynes 1985, 1989; Killworth and McIntyre 1985).

- At larger supercriticalities ($\beta \lesssim 0.30$) equilibration no longer takes place via the mechanism of PV homogenization in the lower layer. Instead, the negative zonal mean gradient of PV in the lower layer is eliminated due to the formation (roll up) of a train of opposite-signed vortices, which remain stable at long times. For narrow channels ($W = 4$ here) vortex roll-up was found to be much more prevalent, even at low supercriticalities, whereas for wide channels ($W = 10$) PV homogenization occurs until $\beta \lesssim 0.15$.
- At low supercriticalities, the maximum wave amplitude in the upper layer is close to 88% of the upper bound (26) obtained from the Held–Shepherd pseudomomentum bound, 88% being the expected ratio from the WGP theory. As the supercriticality increases, and the Held–Shepherd bound switches to a simple enstrophy bound (for $\beta < 1/6$), the maximum wave amplitude remains close to attaining the bound (86–92% for channel width $W \gtrsim 2^{3/4}\pi$). However in the narrow channel simulations, in which the vortex roll-up equilibration method was prevalent, the maximum wave amplitudes attained were considerably smaller (73–82% of the bound (26)).
- New perturbation energy bounds (33), (39) and (40) were found that improved upon that of Shepherd (1993, see his equation 8.2). In the simulations the perturbation energies reached $\approx$80% of the maximum attainable under the known bounds in the wide channel simulations ($W = 10$ here), but were not close to being attained in the narrow channel (e.g. $W = 4$) simulations, suggesting the possibility that the bounds might be further improved.

In summary, the study of nonlinear baroclinic equilibration in Phillips model is clearly of pedagogical importance, both because of the exact scaling behaviour that is revealed, and because it provides a concrete example of an unstable geophysical flow equilibrating via (coarse-grain) PV homogenization. In this work, in addition to extending and simplifying the most important analytical results, the relevance of that analytical work to fully nonlinear flows at finite supercriticality has been demonstrated. It is hoped that the results go some way towards clarifying the insights that can be drawn from Phillips model vis-a-vis real baroclinic flows in the laboratory and in Nature. A companion paper (Willcocks and Esler 2011) deals with the effects caused by Ekman friction acting in each of the two layers. The results there show that while the inviscid equilibrated flow remains relevant in the presence of Ekman friction, it does not determine the long-time "climate" of the model, even when the Ekman friction is vanishingly small.

Acknowledgements

JGE acknowledges support from the UK Natural Environment Research Council NE/G003122/1, and BTW the support of an EPSRC studentship.

References

Abramowitz, M. and Stegun, I., *Handbook of Mathematical Functions*, 1972. (New York: Dover).

Arnol'd, V.I., On an a priori estimate in the theory of hydrodynamic stability. *Izv. Vyssh. Uchebn. Zaved. Mat.*, 1966, **54**, 3–5 (English transl.: Am. Math. Soc. Transl., Series 2, 1969, **79**, 267–269).

Berloff, P., Kamenkovich, I. and Pedlosky, J., A mechanism of formation of multiple zonal jets in the ocean. *J. Fluid Mech.* 2009, **628**, 395–425.

Boville, B., Amplitude vacillation on a β-plane. *J. Atmos. Sci.* 1981, **38**, 609–618.

Drazin, P.G., Non-linear baroclinic instability of a continuous zonal flow. *Q. J. R. Met. Soc.* 1970, **96**, 667–676.

Esler, J.G., Simple models of wave packets in an equilibrated baroclinic system. *J. Atmos. Sci.* 1997, **54**, 2820–2849.

Esler, J.G., The turbulent equilibration of an unstable baroclinic jet. *J. Fluid Mech.* 2008, **599**, 241–268.

Esler, J.G. and Haynes, P.H., Mechanisms for wave packet formation and maintenance in a quasi-geostrophic two-layer model. *J. Atmos. Sci.* 1999, **56**, 2457–2489.

Gauthier, P., Effect of detuning on the development of marginally unstable baroclinic vortices. *J. Atmos. Sci.* 1990, **47**, 999–1011.

Haynes, P.H., Nonlinear instability of a Rossby-wave critical layer. *J. Fluid Mech.* 1985, **161**, 493–511.

Haynes, P.H., The effect of barotropic instability on the nonlinear evolution of a Rossby-wave critical layer. *J. Fluid Mech.* 1989, **207**, 231–266.

Killworth, P.D. and McIntyre, M.E., Do Rossby-wave critical layers absorb, reflect or over-reflect? *J. Fluid Mech.* 1985, **161**, 449–492.

Maslowe, S., Critical layers in shear flows. *Ann. Rev. Fluid Mech.* 1986, **18**, 405–432.

Mu, M., Zeng, Q., Shepherd, T.G. and Liu, Y., Nonlinear stability of multilayer quasi-geostrophic flow. *J. Fluid Mech.* 1995, **264**, 165–184.

Pedlosky, J., Finite amplitude baroclinic waves. *J. Atmos. Sci.* 1970, **27**, 15–30.

Pedlosky, J., On secondary baroclinic instability and the meridional scale of motion in the ocean. *J. Phys. Oceanogr.* 1975, **5**, 603–607.

Pedlosky, J., Finite-amplitude baroclinic waves at minimum critical shear. *J. Atmos. Sci.* 1982a, **39**, 555–562.

Pedlosky, J., A simple model for nonlinear critical layers in an unstable baroclinic wave. *J. Atmos. Sci.* 1982b, **39**, 2119–2127.

Pedlosky, J., *Geophysical Fluid Dynamics*, 1987. (New York: Springer-Verlag).

Phillips, N.A., A simple three-dimensional model for the study of large-scale extratropical flow patterns. *J. Met.* 1951, **8**, 381–394.

Phillips, N.A., Energy transformations and meridional circulations associated with simple baroclinic waves in a two-level quasi-geostrophic model. *Tellus* 1954, **6**, 273–286.

Rhines, P. and Young, W., How rapidly is a passive scalar mixed within closed streamlines? *J. Fluid Mech.* 1983, **133**, 133–145.

Shepherd, T.G., Nonlinear saturation of baroclinic instability. Part I: the two-layer model. *J. Atmos. Sci.* 1988, **45**, 2014–2025.

Shepherd, T.G., Symmetries, conservation laws, and Hamiltonian structure in geophysical fluid dynamics. *Adv. Geophys.* 1990, **32**, 287–338.

Shepherd, T.G., Nonlinear saturation of baroclinic instability. Part III: Bounds on the energy. *J. Atmos. Sci.* 1993, **50**, 2697–2709.

Stewartson, K., The evolution of the critical layer of a Rossby wave. *Geophys. Astrophys. Fluid Dyn.* 1978, **9**, 185–200.

Vallis, G.K., *Atmospheric and Oceanic Fluid Dynamics*, 2006. (Cambridge: Cambridge University Press).

Warn, T. and Gauthier, P., Potential vorticity mixing by marginally unstable baroclinic disturbances. *Tellus* 1989, **41A**, 115–131.

Warn, T. and Warn, H., The evolution of a nonlinear critical level. *Stud. Appl. Math.* 1978, **59**, 37–71.

Willcocks, B.T. and Esler, J.G., Nonlinear baroclinic equilibration in the presence of Ekman friction. *J. Phys. Oceanogr.* 2011, doi: 10.1175/JPO-D-11-0112.

Appendix A: Switching between nondimensionalizations

In section 1, it was pointed out that both WG89 and Shepherd (1988, 1993) used a "degenerate" nondimensionalization of Phillips model when deriving their results, following Pedlosky (e.g. 1987). Our view is that Pedlosky's nondimensionalization

makes the results of WG89 and Shepherd appear more complicated than necessary. In particular, the fact that several important results depend primarily on a single parameter (our β) with the other nondimensional parameter (our W) scaling trivially, is obscured if Pedlosky's precedent is followed.

Nevertheless it is clearly necessary to be able to switch between the two nondimensionalizations in order to compare results. The degeneracy in Pedlosky's treatment follows from introducing an additional velocity scale U_0 that is distinct from the initial upper layer velocity U, and is not defined explicitly. This additional velocity scale allows the three nondimensional quantities

$$\tilde{\beta} = \frac{\beta^* L_y^2}{U_0}, \quad \tilde{F} = \frac{1}{2}\frac{L_y^2}{L_D^2}, \quad \tilde{U} = \frac{U}{U_0} \tag{A.1}$$

to be defined, where tildes will henceforth denote quantities under Pedlosky's nondimensionalization. Note that the factor of two in the definition of $\tilde{F}$ can be traced to our definition of the internal Rossby radius L_D, where (following Vallis 2006, see his equation 5.191) our definition is the natural scale appearing in the baroclinic PV equation. Our parameters β and W can be expressed in terms of those of Pedlosky using

$$\beta = \frac{\tilde{\beta}}{2\tilde{F}\tilde{U}}, \quad W = \sqrt{2\tilde{F}}.$$

The above relations allow our results to be easily translated to the Pedlosky form, provided that the dimensions of the quantity being treated are also accounted for. For example, in our treatment, zonal mean perturbation entropy Z'/L has dimensions $L_D^{-1}U^2$, whereas under the Pedlosky scaling $\tilde{Z}'$ (which is defined as a zonal mean quantity) has dimensions $L_y^{-1}U_0^2$. This means that $Z'/\mathrm{LW} = 2\tilde{F}\tilde{Z}'/\tilde{U}^2$, which allows (24) to be converted to

$$\tilde{Z}' \leq \frac{1}{12}\begin{cases} 4\tilde{\beta}(\tilde{F}\tilde{U} - \tilde{\beta}) & \frac{1}{2} \leq \tilde{\beta}/\tilde{F}\tilde{U} \leq 1, \\ \tilde{F}^2\tilde{U}^2 & 0 < \tilde{\beta}/\tilde{F}\tilde{U} < \frac{1}{2} \end{cases}$$

recovering equation (5.6) of Shepherd (1988) for the perturbation enstrophy bound.

Similarly, comparing the dimensions of the zonal mean perturbation energy here and in the Pedlosky form leads to $E'/\mathrm{LW} = \tilde{E}'/\tilde{U}^2$. This allows (33) to be written

$$\tilde{E}' \leq \begin{cases} \dfrac{\tilde{\beta}}{6\tilde{F}}\left(\tilde{U}\tilde{F} - \tilde{\beta}\right)\left(1 + \dfrac{6(\tilde{U}\tilde{F} - \tilde{\beta})}{\tilde{\beta}(\tilde{F}+6)}\right) & \dfrac{1}{2} - \dfrac{3}{\tilde{F}} \leq \tilde{\beta}/\tilde{F}\tilde{U} < 1, \\ \dfrac{1}{24}\tilde{U}^2\left(\tilde{F}+6\right) & 0 < \tilde{\beta}/\tilde{F}\tilde{U} < \dfrac{1}{2} - \dfrac{3}{\tilde{F}}. \end{cases} \tag{A.2}$$

Compared with equation (8.2) of Shepherd (1993) it is again clear that the useful bound on the upper line is an improvement on Shepherd's result. Applying the conversion process in reverse to Shepherd's (8.2) results in equation (34).

Appendix B: Solution of the lower layer PV advection equation (17)

Here, a re-working of WG89's solution to the lower layer PV advection equation ((17) above) is presented. Equation (17) is

$$\left(\partial_\eta - \Psi_y\partial_x + \Psi_x\partial_y\right)Q = 0, \quad \text{where } \Psi = \cos(k_m x)\cos(\pi y/W),$$

and it has initial condition

$$Q(x, y, 0) = -y.$$

Equation (17) is a homogeneous linear partial differential equation and its solution can be obtained directly using the method of characteristics,

$$Q(x(x_0, y_0, \eta), y(x_0, y_0, \eta), \eta) = -y_0,$$

where

$$\frac{\mathrm{d}x}{\mathrm{d}\eta} = -\Psi_y(x, y) \quad \text{and} \quad \frac{\mathrm{d}y}{\mathrm{d}\eta} = \Psi_x(x, y), \quad \text{with } x(0) = x_0,\ y(0) = y_0. \tag{B.1}$$

The physical interpretation of the characteristic equations is that a fluid parcel with coordinates (x_0, y_0) at $\eta = 0$ has coordinates (x, y) at scaled time η, and carries its initial PV value with it to its new location, hence $Q(x, y, \eta) = -y_0$. The equations (B.1) are recognisable as Hamilton's equations and, by analogy since it does not depend explicitly on η, Ψ is easily shown to be an invariant (cf. the Hamiltonian). Physically this recovers the fact that fluid particles in steady flow move along streamlines ($\Psi =$ constant). The initial conditions consequently provide the identity

$$\Psi(x, y) = \cos(k_m x)\cos(\pi y/W) = \cos(k_m x_0)\cos(\pi y_0/W) = \Psi_0(x_0, y_0). \tag{B.2}$$

The identity (B.2) can be used to rewrite the second equation of (B.1) as

$$\frac{\mathrm{d}y}{\mathrm{d}\eta} = \mp k_m m_0^{1/2}\left(1 - m_0^{-1}\sin^2(\pi y/W)\right)^{1/2}, \quad y(0) = y_0, \tag{B.3}$$

where $m_0 = 1 - \Psi_0^2$ can be treated as a constant. The negative branch is taken in the subdomain $x \in [-\pi/2k_m, \pi/2k_m]$ followed by the positive branch in $x \in [\pi/2k_m, 3\pi/2k_m]$ etc., i.e. the lower layer flow consists of disjoint cells as illustrated in figure 2(a). Henceforth the focus will be on the cell $(x, y) \in [-\pi/2k_m, \pi/2k_m] \times [-W/2, W/2]$, with the full solution easily constructed from this cell using the symmetry relation

$$Q\left(x + \frac{\pi}{2k_m}, y, t\right) = Q\left(\frac{\pi}{2k_m} - x, y, t\right).$$

Equation (B.3) can be integrated directly, using the definitions of elliptic integrals (e.g. Abramowitz and Stegun 1972) to give

$$\mathrm{F}\left(\sin^{-1}\left(m_0^{-1/2}\sin\left(\frac{\pi y}{W}\right)\right)|m_0\right) + \frac{k_m\pi}{W}\eta = \mathrm{F}\left(\sin^{-1}\left(m_0^{-1/2}\sin\left(\frac{\pi y_0}{W}\right)\right)|m_0\right), \tag{B.4}$$

where

$$\mathrm{F}(z|m) = \int_0^z \frac{1}{(1 - m\sin^2 t)^{1/2}}\,\mathrm{d}t$$

is the incomplete elliptic integral of the first kind. It is helpful to note that $m^{-1/2}\mathrm{F}(z|m^{-1}) = \mathrm{F}(\sin^{-1}(m^{-1/2}\sin z)|m)$. Equation (B.4) can be used to obtain the fluid parcel latitude y in terms of its initial position (x_0, y_0). Alternatively, the fact that $m = m(\Psi)$ is an invariant can be exploited, by substituting $m = 1 - \Psi^2 = 1 - \cos^2(k_m x)\cos^2(\pi\, y/W)$ for m_0 in (B.4), and the initial latitude y_0 can then be found in terms of the current position (x, y). It is of course the latter result that is needed, since the initial latitude y_0 provides the solution of equation (17), through $Q(x, y, \eta) = -y_0$. Applying the Jacobi elliptic function $sn(\cdot|m)$ to (B.4), and using the following standard identities

$$\mathrm{sn}(F(z|m)|m) = \sin z, \quad \mathrm{cn}(F(z|m)|m) = \cos z, \quad \mathrm{dn}(F(z|m)|m) = (1 - m\sin^2 z)^{1/2},$$

$$\mathrm{sn}(u + v|m) = \frac{\mathrm{sn}(u|m)\mathrm{cn}(v|m)\mathrm{dn}(v|m) + \mathrm{sn}(v|m)\mathrm{cn}(u|m)\mathrm{dn}(u|m)}{1 - m\mathrm{sn}^2(u|m)\mathrm{sn}^2(v|m)}$$

results directly in the solution (18) given in section 3.

Numerical quadrature of the integral in (14) is best effected by making the coordinate transformation $(x, y) \to (\alpha, m)$ where $m(x, y)$ is defined above and†

$$\alpha(x, y) = \frac{k_m \pi}{W}\eta + F\Big(\sin^{-1}\Big(m^{-1/2}\sin\Big(\frac{\pi y}{W}\Big)\Big)\Big|m\Big). \tag{B.5}$$

Applying the transformation gives

$$Q = -\frac{W}{\pi}\sin^{-1}\big(m^{1/2}\mathrm{sn}(\alpha|m)\big),$$
$$y = \frac{W}{\pi}\sin^{-1}\Big(m^{1/2}\mathrm{sn}\Big(\alpha - \frac{k_m\pi}{W}\eta\,|m\Big)\Big),$$

which together with the Jacobian

$$\frac{\partial(x, y)}{\partial(\alpha, m)} = \frac{W}{2k_m\pi}(1 - m)^{-1/2}$$

allows the integral in (14) to be written in the form $I(z)$ given in (19). Note that the limit $\mathrm{K}(m) = \mathrm{F}(\pi/2|m)$ in the inner integral corresponds to integrating over only a quarter of a circulation "cell" defined above, with the integral over the full cell being four times greater, since the integrand has symmetries in both x- and y-directions.

†Note that WG89 do not explicitly define their (equivalent) variable α.

Appendix C: Details of the derivation of the bounds (39) and (40)

Here a few intermediate steps used to obtain the perturbation energy bounds (39) and (40) are given. If the extremal functions (36) and (38) are inserted into the expression (30), the following bound is obtained:

$$\begin{aligned} E' \leq \frac{\mathrm{LW}}{2}\left(1 + 2\mu\alpha_2 q - \frac{4q\alpha_2\beta + 4\mu\left(1 + \left(\frac{1}{2} - \beta\right)q\right)}{q+2} - \frac{4q^2\beta^2}{(q+2)^2}\right) \\ + \frac{\mathrm{LW}^3}{24}\frac{\left(1 + \left(\frac{1}{2} - \beta\right)q\right)^2}{q+2} \\ + \frac{\mathrm{LW}^2}{8}\frac{\sqrt{2}\sqrt{q+2}\left(2\beta q + \alpha_2(q+2) - \mu(q+2)^2\right)^2}{\sqrt{q}(q+2)^2}\coth\left(\sqrt{\tfrac{1}{2}+\tfrac{1}{q}}\,\frac{W}{2}\right). \end{aligned} \quad \text{(C.1)}$$

The aim, as in section 3.3, is to minimize the bound with respect to (μ, α_2, q) over the domain $\mathbb{R} \times \mathbb{R} \times (0, \infty)$. The problem is again quadratic in μ and α_2, hence the critical point can be determined as function of q by solving a linear system. The solution of the linear system is found to be

$$\begin{aligned} \mu_c(q) &= \frac{4\beta q\sqrt{q} - \sqrt{2}\sqrt{q+2}\,(1 + (\frac{1}{2} + \beta)q)W\coth\left(\sqrt{\frac{1}{2}+\frac{1}{q}}\,\frac{W}{2}\right)}{(q+2)\left(2\sqrt{q} - \sqrt{2}\sqrt{q+2}\,W\coth\left(\sqrt{\frac{1}{2}+\frac{1}{q}}\,\frac{W}{2}\right)\right)}, \\ \alpha_{2c}(q) &= \frac{\left(1 + (\frac{1}{2} - \beta)q\right)\left(4\sqrt{q} - \sqrt{2}\sqrt{q+2}\,W\coth\left(\sqrt{\frac{1}{2}+\frac{1}{q}}\,\frac{W}{2}\right)\right)}{(q+2)\left(2\sqrt{q} - \sqrt{2}\sqrt{q+2}\,W\coth\left(\sqrt{\frac{1}{2}+\frac{1}{q}}\,\frac{W}{2}\right)\right)}. \end{aligned} \quad \text{(C.2)}$$

Insertion of (C.2) into (C.1) leads, after some working, to equation (39).

The approximation to (39) given by (40) is found by first writing

$$\mathcal{G}(q, \beta, W) = \mathcal{G}(1/\epsilon + \tilde{q}, \tfrac{1}{2} - \epsilon^2, W).$$

The resulting expression is expanded in powers of ϵ, and truncated at $\mathrm{O}(\epsilon^3)$. The value of $\tilde{q}$ for which the truncated expression is minimized is easily shown to be $\tilde{q} = -J(W)$, where $J(W)$ is given in section 3. The bound (40) follows immediately.